Land surface microwave emissivities derived from AMSR-E and MODIS measurements with advanced quality control

Jean-Luc Moncet, Pan Liang, John F. Galantowicz, Alan E. Lipton, Gennady Uymin, Catherine Prigent, Christopher Grassotti

Land surface microwave emissivities derived from AMSR-E and MODIS measurements with advanced quality control

Jean-Luc Moncet,[1] Pan Liang,[1] John F. Galantowicz,[1] Alan E. Lipton,[1] Gennady Uymin,[1] Catherine Prigent,[2] and Christopher Grassotti[1,3]

Received 2 December 2010; revised 8 April 2011; accepted 10 May 2011; published 16 August 2011.

[1] A microwave emissivity database has been developed with data from the Advanced Microwave Scanning Radiometer-EOS (AMSR-E) and with ancillary land surface temperature (LST) data from the Moderate Resolution Imaging Spectroradiometer (MODIS) on the same Aqua spacecraft. The primary intended application of the database is to provide surface emissivity constraints in atmospheric and surface property retrieval or assimilation. An additional application is to serve as a dynamic indicator of land surface properties relevant to climate change monitoring. The precision of the emissivity data is estimated to be significantly better than in prior databases from other sensors due to the precise collocation with high-quality MODIS LST data and due to the quality control features of our data analysis system. The accuracy of the emissivities in deserts and semiarid regions is enhanced by applying, in those regions, a version of the emissivity retrieval algorithm that accounts for the penetration of microwave radiation through dry soil with diurnally varying vertical temperature gradients. These results suggest that this penetration effect is more widespread and more significant to interpretation of passive microwave measurements than had been previously established. Emissivity coverage in areas where persistent cloudiness interferes with the availability of MODIS LST data is achieved using a classification-based method to spread emissivity data from less-cloudy areas that have similar microwave surface properties. Evaluations and analyses of the emissivity products over homogeneous snow-free areas are presented, including application to retrieval of soil temperature profiles. Spatial inhomogeneities are the largest in the vicinity of large water bodies due to the large water/land emissivity contrast and give rise to large apparent temporal variability in the retrieved emissivities when satellite footprint locations vary over time. This issue will be dealt with in the future by including a water fraction correction. Also note that current reliance on the MODIS day-night algorithm as a source of LST limits the coverage of the database in the Polar Regions. We will consider relaxing the current restrictions as part of future development.

Citation: Moncet, J.-L., P. Liang, J. F. Galantowicz, A. E. Lipton, G. Uymin, C. Prigent, and C. Grassotti (2011), Land surface microwave emissivities derived from AMSR-E and MODIS measurements with advanced quality control, *J. Geophys. Res.*, *116*, D16104, doi:10.1029/2010JD015429.

1. Introduction

[2] Microwave measurements from space have great potential to contribute to the detection and understanding of climate trends, due largely to their unique ability to detect surface and atmosphere properties through clouds. Microwave products minimize the "cloud bias" that occurs with infrared-based analysis in which the data sets systematically exclude cloudy areas. Cloud biases can be particularly damaging when analyzing trends in parameters like land surface temperature (LST) and tropospheric water vapor, which are strongly correlated with cloudiness. Climate-quality microwave retrievals of surface and lower tropospheric parameters have thus far been largely restricted to ocean areas, due to the challenges of distinguishing changes in surface temperature, water vapor, clouds, and precipitation from the spatial and temporal variability of the microwave emissivity over land.

[3] The work reported here was directed at overcoming this limitation by leveraging products from several NASA Earth Observing System (EOS) instruments to create an emissivity database to facilitate the use of data from the Advanced Microwave Scanning Radiometer-EOS (AMSR-E) and other conically scanning microwave sensors for detecting climate sensitive parameters. The particular focus was on meeting

[1] Atmospheric and Environmental Research, Inc., Lexington, Massachusetts, USA.
[2] Laboratoire d'Etudes du Rayonnement et de la Matière en Astrophysique, CNRS, Observatoire de Paris, Paris, France.
[3] Now at I.M. Systems Group, Inc., Center for Satellite Applications and Research, NESDIS, NOAA, Camp Springs, Maryland, USA.

0148-0227/11/2010JD015429

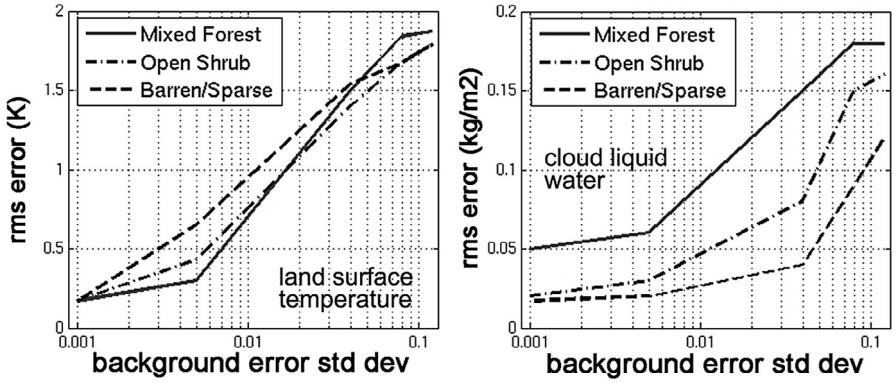

Figure 1. Simulated retrieval quality improvement (rms error) as a function of background error standard deviation (a priori knowledge) of surface emissivity (as scaled to the 19/24 GHz H polarization standard deviation), for a one-dimensional variation algorithm and a generic conically scanning microwave imager/sounder. Results are for surface types with relatively high, medium, and low emissivities (mixed forest, open shrub, and barren/sparse, respectively).

the strict accuracy requirements for use of the emissivity as an input to variational algorithms for retrieval or assimilation of precipitable water, liquid water, and surface temperature in cloudy conditions. These applications require, for each satellite overpass, an estimate of the local surface emissivity and the associated error covariance, based on the recent history of emissivities at a given location. The emissivity database is also valuable, in its own right, as a tool for diagnosing land surface properties, in relation to climate, weather, and land use practices.

[4] The emissivity retrieval methodology used in this project has its heritage in the work of *Prigent et al.* [2006, 1997, 1999] who derived global maps of monthly mean land surface emissivities from Defense Meteorological Satellite Program (DMSP) Special Sensor Microwave/Imager (SSM/I) data and ancillary cloud and LST products from the International Satellite Cloud Climatology Project (ISCCP) [*Rossow and Schiffer*, 1999] and atmospheric data from numerical weather prediction (NWP) models. The present work expands the previous analysis by adding highly valuable information from the EOS Aqua spacecraft sensors AMSR-E and the Moderate Resolution Imaging Spectroradiometer (MODIS). MODIS is used in our analysis to provide estimates of LST and cloud cover in the AMSR-E fields of view ("footprints"). Here we benefit from the excellent temporal and spatial collocation between AMSR-E and MODIS on the Aqua platform. This factor is important for maintaining a high level of consistency between the different data sources in rapidly changing atmospheric and surface thermal conditions. In addition, AMSR-E carries low-frequency channels (7 and 11 GHz) that are not available from the SSM/I instrument. We did not use the 7 GHz channel for this study because of widespread radio frequency interference (RFI) over land [*Njoku et al.*, 2005]. The 11 GHz information (which is not extensively affected by RFI) is largely unaffected by clouds and water vapor and constitutes a powerful resource both for improving accuracy of MW LST retrievals (over vegetated surfaces, where differences between infrared and microwave emission temperature are expected to be minimal, especially at night) and for monitoring temporal changes in the state of the surface. Unlike the DMSP satellites, which are in early morning/evening orbits, the Aqua satellite has a nominal 01:30/13:30 equatorial crossing time, which is well timed for capturing the amplitude of the diurnal cycle. The large thermal contrasts between the surface skin temperatures (sensed by MODIS) and subsurface temperatures, at the time of the Aqua satellite overpass, allowed us to provide an indication that the subsurface microwave penetration is much more widespread than previously thought [*Prigent et al.*, 1999]. AMSR-E also has advantages over SSM/I with respect to the density of spatial sampling and the availability of footprint-matched measurements at all frequencies [*Ashcroft and Wentz*, 2000].

[5] We devote a substantial portion of this paper to analysis of factors that affect emissivity database quality and to procedures for enhancing the quality of our products. The value of the database for variational assimilation and retrieval is highly sensitive to the database quality. In one-dimensional variation retrievals with simulated data, retrieval errors for land surface temperature and cloud liquid water were reduced by about a factor of four as background emissivity error standard deviation was reduced from 0.1 to 0.005, while errors for precipitable water had a smaller, but still significant sensitivity (Figure 1).

2. Emissivity Retrieval Methodology

2.1. Algorithms

2.1.1. Background

[6] Our formulation of microwave radiative transfer over land treats surface reflectivity as specular. The emissivity errors introduced by this approximation has been shown to be generally less than 1% for nadir views, and the errors would be considerably less for the view angles of ASMR-E and SSM/I (55° and 53°, respectively), and particularly in the more transparent channels [*Karbou and Prigent*, 2005]. The brightness temperatures (TB) measured by satellite-borne microwave sensors at a frequency ν and polarization p in nonscattering atmospheres are modeled as

$$T^B_{\nu,p} = T^{\uparrow}_{\nu} + \tau_{\nu}\left[\varepsilon_{\nu,p}T_{e,\nu} + \left(1-\varepsilon_{\nu,p}\right)T^{\downarrow}_{\nu}\right], \tag{1a}$$

$$= \left(T_\nu^\uparrow + \tau_\nu T_\nu^\downarrow\right) + \varepsilon_{\nu,p}\left(\tau_\nu T_{e,\nu} - \tau_\nu T_\nu^\downarrow\right) \quad (1b)$$

$$T_{\nu,p}^B = A_\nu + \varepsilon_{\nu,p}\left(B_\nu T_{e,\nu} + C_\nu\right), \quad (1c)$$

where τ_ν is the total atmospheric transmittance along the sensor line of sight, $T_\nu^\uparrow$ and $T_\nu^\downarrow$ represent the upwelling and downwelling atmospheric emission, respectively, and $\varepsilon_{\nu,p}$ is the surface emissivity. The attenuated cosmic background is included in the downwelling emission term. The A, B and C terms in (1c) are abbreviations of the corresponding terms in (1b). Since we are dealing exclusively with conically scanning imagers, the dependence of these variables on sensor viewing angle (which is approximately constant) is omitted from our notation. In (1), $T_{e,\nu}$ is the effective emission temperature of the surface. The dependence of T_e on ν is often neglected, but it should be taken into account when 1) emission from underneath the surface "skin" layer contributes significantly to the outgoing surface radiation, 2) we consider a range of ν where the emission depth varies, and 3) there are large thermal vertical gradients (within the ground, ground cover, and/or canopy). There is no evidence thus far in our analyses that T_e should also depend on polarization.

[7] Microwave surface emissivity estimation from spaceborne imaging sensor data relies on atmospheric data from other sources to provide estimates of the A, B and C terms in (1c). The atmosphere may be highly variable, both spatially and temporally. For this reason, it could be advantageous to derive the water vapor and temperature profiles from independent, well-collocated satellite measurements, if one can overcome any significant sensor intercalibration issues. At this stage of development, we rely on global NWP models to provide this information. The atmospheric absorption model used in this study is from *Rosenkranz* [1998] [see also *Liebe et al.*, 1992]. Retrieved land surface emissivities may depend somewhat on the model used for producing an atmospheric correction, which is an important consideration in the subsequent application of the emissivity database to atmospheric retrieval or satellite data assimilation. In the spectral regime of interest, existing models [e.g., *Payne et al.*, 2008; *Smith et al.*, 2001] differ mainly in the specification of the 22.235 GHz water vapor line width and the strength of the water vapor self and foreign-broadened continua. Errors in the width of the water vapor line may have significant impact on measurements taken right at the line center (e.g., SSM/I) and only have a minor impact at 23.8 GHz (e.g., AMSR-E). The impact of continuum errors is largest at 89 and 37 GHz (in horizontal polarization). Until the different models converge, the same molecular absorption physics should be used in generating the emissivity data and in the subsequent use of those emissivities for atmospheric characterization.

[8] The emissivity retrieval method is designed to operate in clear-sky conditions, in part because of our inability to correct the microwave measurements for the impact of clouds, due to the lack of reliable independent estimates of the relevant cloud physical properties and the uncertainties in the modeling of the radiative impact of clouds on the microwave brightness temperatures. Another reason is that there is no adequate source of LST data under cloudy conditions. Emissivities retrieved from clear-sky data can then be used in subsequent cloudy conditions to aid with retrieval of other variables (e.g., LST and water vapor), provided there are mechanisms to screen for abrupt changes in emissivity.

2.1.2. Nonpenetration Approximation

[9] A first approach, used by *Prigent et al.* [1997] for deriving surface emissivity from SSM/I measurements, assumes that the surface emits at the same temperature at all frequencies, i.e. $T_{e,\nu} = T_s$, where T_s is the surface skin temperature, obtained from infrared measurements (i.e., LST). In this case, an emissivity estimate at each microwave frequency and polarization is derived from the microwave measured brightness temperatures using (1c) rearranged as

$$\varepsilon_{\nu,p} = \left(T_{\nu,p}^B - A_\nu\right) \Big/ \left(B_\nu T_s + C_\nu\right). \quad (2)$$

Temporal averaging is applied to minimize random errors in the instantaneous emissivity retrievals, arising mostly from the specification of T_s and the coefficients A, B and C. This approach is herein called the nonpenetration approximation (NPA).

[10] Emissivity retrievals from (2) can provide straightforward results over highly absorbing (e.g., moderately to highly vegetated) areas or, over all areas, when the surface/subsurface medium is close to isothermal (i.e., infrared and microwave emission source temperatures are roughly equal). Over highly penetrating surfaces such as sandy deserts, where subsurface emission is dominant, the solution provided by (2) is contaminated by the systematic differences between T_s and $T_{e,\nu}$ and does not have a straightforward physical meaning, although such a solution may still be useful for atmospheric retrievals in regions where there is little day-to-day change in the thermal structure of the surface. Biases in the retrieved emissivities caused by systematic differences between T_s and $T_{e,\nu}$ can be partially eliminated by averaging measurements taken at different times of day, but it is best to revert to the more general form of radiative transfer provided in (1).

2.1.3. Penetration Time Series

[11] Surface emissivity characterization in areas where microwave penetration is significant is based on an approach tested by *Prigent et al.* [1999], which relates the thermal cycle at some depth in the medium to the diurnal forcing at the surface by applying the one-dimensional heat flow equation for a homogeneous medium:

$$\kappa \frac{\partial^2 T(d,t)}{\partial d^2} = \frac{\partial T(d,t)}{\partial t}, \quad (3)$$

where $T(d, t)$ is temperature at depth d and time t, and κ is the thermal diffusivity of the medium. The solution to (3) for a semi-infinite medium under periodic surface heating (with 24 h period), can be expressed in terms of cosine series,

$$T(\alpha,t) = T_0 + \sum_n A_n \exp\left(-\alpha\sqrt{n}\right)\cos\left(n\omega_0 t + \phi_n - \alpha\sqrt{n}\right), \quad (4)$$

where $\omega_0 = 2\pi/86400$ [s^{-1}] and $\alpha = d\sqrt{\omega_0/2\kappa}$. At the surface ($\alpha = 0$), and (4) simplifies to

$$T_s(t) = T(0,t) = T_0 + \sum_n A_n \cos(n\omega_0 t + \phi_n). \quad (5)$$

T_0 represents the mean surface temperature over the time period analyzed, and A_n, and ϕ_n are the amplitude and phase of the nth term in the cosine series representation of the periodic surface forcing.

[12] *Prigent et al.* [1999] applied (4) as $T_{e,\nu}(t) \approx T(\alpha_\nu, t)$, with each frequency thus mapping to a certain α_ν. In this work, we applied an alternative model, formulated in terms of temperature averaged from the top (α_0) to the bottom (α) of a layer, considering that each frequency responds to a range of depths:

$$\begin{aligned} T_e(\alpha_0, \alpha, t) = T_0 + \sum_n \frac{A_n \exp(-\alpha_0\sqrt{n})}{2\Delta\alpha\sqrt{n}} \left[\cos\left(n\omega_0 t + \varphi_n - \alpha_0\sqrt{n}\right)\right. \\ \left. + \sin\left(n\omega_0 t + \varphi_n - \alpha_0\sqrt{n}\right)\right] \\ - \sum_n \frac{A_n \exp(-\alpha\sqrt{n})}{2\Delta\alpha\sqrt{n}} \left[\cos\left(n\omega_0 t + \varphi_n - \alpha\sqrt{n}\right)\right. \\ \left. + \sin\left(n\omega_0 t + \varphi_n - \alpha\sqrt{n}\right)\right], \end{aligned} \tag{6}$$

where $\Delta\alpha = \alpha - \alpha_0$. When applying (6) to microwave measurements, we have generally used $\alpha_0 = 0$ and refer to α as α_ν, so $T_{e,\nu}(t) \approx \overline{T}(0, \alpha_\nu, t)$. Preliminary data suggested that (6), with $\alpha_0 = 0$, provided a better fit to clear-sky observations than (4).

[13] Equations (5) and (6) provide a one-parameter (α_ν) link between $T_s(t)$ and $T_{e,\nu}(t)$. Although the assumptions inherent in these formulations are major simplifications of the actual properties of terrestrial surfaces, this construct has been shown to be a useful first-order quantification of penetration effects, wherein α_ν represents spatial and temporal variations in penetration. The assumptions are tested in the quality control process using the model fit error [*Galantowicz et al.*, 2011].

[14] A solution for the model parameters is obtained, following *Prigent et al.* [1999], by first fitting (5) (with $n = 1, 2$) by nonlinear least squares to multiday 85–89 GHz vertical polarization atmosphere-corrected TBs to estimate the surface phase parameters $\{\phi_1, \phi_2\}$. This phase determination uses these highest-frequency channels because they have the least penetration and the least affected by phase lag relative to the surface. Next, with $\{\phi_1, \phi_2\}$ held constant, (5) is fit to the collected MODIS LSTs, solving for $\{T_0, A_1, A_2\}$ and completing the surface parameter set. Last, we solve for $\{\varepsilon_{\nu,V}, \varepsilon_{\nu,H}\}$ (where V = vertical and H = horizontal) and α_ν by adjusting the three parameters until the best match is obtained between the output of the model described by (6) and sets of effective emitting temperatures estimates derived from V and H satellite observations at clear-sky observation times, i:

$$\begin{aligned} T^i_{e,\nu} &= \left[\left(T^B_{\nu,p} - T^\uparrow_\nu\right) \Big/ \tau_\nu - \left(1 - \varepsilon_{\nu,p}\right) T^\downarrow_\nu\right] \Big/ \varepsilon_{\nu,p} \\ &= \frac{1}{B_\nu}\left(\frac{T^B_{\nu,p} - A_\nu}{\varepsilon_{\nu,p}} - C_\nu\right), \end{aligned} \tag{7}$$

where $\varepsilon_{\nu,p}$ are the time-averaged emissivities to be solved for at each polarization. Data from multiple satellites are required to adequately sample the diurnal cycle. Current restrictions are that the surface emissivity be stable through the fitting period and that the surface be also thermally stable. The length of the fitting period can be varied (e.g., a few days to one month or more) to balance the capture of surface dynamics against reduction of random errors and compensation for frequent cloudiness. A more detailed description of the process currently in use where high penetration is suspected is given by *Galantowicz et al.* [2011]. This approach represented by (5) and (6) is called penetration time series (PTS) in the following discussions.

2.2. Data Sources

[15] The AMSR-E uses a conical scan pattern at an Earth incidence angle (EIA) of 55°, with ascending and descending nominal equator crossing times (ECT) 13:30 and 01:30 local. There are V- and H-polarized channels centered at 6.925, 10.65, 18.7, 23.8, 36.5, and 89 GHz [*Kawanishi et al.*, 2003], abbreviated here as 7, 11, 19, 24, 37, and 89 GHz, respectively. The radiometric data used here were taken over calendar year 2003, and are from the V09 version of the AMSR-E/Aqua L2A processing [*Ashcroft and Wentz*, 2003]. In this data set, all channels have been spatially averaged to match a common spatial response pattern (footprint) [*Ashcroft and Wentz*, 2000]. For this work, we used data matched to 51 km × 29 km footprint size (mean spatial resolution = 38 km) sampled at 10 km intervals along scan. All channels except 7 GHz are available at this resolution. The spatial averaging reduces random instrument noise to <0.15 K (rms) at center of scan for all frequencies (or ~0.0005 in terms of equivalent retrieved emissivity standard deviation) before Earth gridding.

[16] The results discussed here were derived with atmospheric temperature and water vapor profiles from the 1° National Centers for Environmental Prediction (NCEP) Global Data Assimilation System (GDAS) analysis [*Kanamitsu*, 1989; *Kalnay et al.*, 1990]. The 6-hourly NWP product was interpolated to the local time of the Aqua overpass and to the center of the AMSR-E footprints. The GDAS analysis terrain elevations were adjusted to the GTOPO30 30-arc-s terrain (available from U.S. Geological Survey, http://eros.usgs.gov/#/Find_Data/Products_and_Data_Available/gtopo30_info), spatially averaged to AMSR-E footprint resolution, and atmospheric water vapor was corrected for the elevation difference.

[17] LST data and cloud flags used in our AMSR-E processing were obtained from Version V004 of the 5 km Level-3 gridded product from the MODIS day-night algorithm [*Wan*, 1999, 2008]. The MODIS LST algorithm makes use of Version V004 of the MODIS cloud mask [*Ackerman et al.*, 1998, 2006]. Our preprocessing uses a threshold of the local temporal LST standard deviation to filter out LST data potentially affected by residual cloud. The filter algorithm from *Wan* [2008] was modified to use the same threshold regardless of surface type, so we would not need to process surface type data, and our threshold (5 K) was subjectively chosen by inspecting images of filtered LSTs and seeking to eliminate any ring of low LST values around cloudy areas. This filter would tend to be less effective at locations where there are few samples in the time series—where cloud cover is persistent and few LST reports pass the initial cloud masking.

[18] A snow/ice flag was adopted from the monthly AMSR-E EASE-gridded land products (AE_Land_3) snow water equivalent [*Kelly et al.*, 2004]. A flag for RFI con-

tamination of the 11 GHz channel is included, obtained from a global (0.25° × 0.25°) static map generated by *Njoku et al.* [2005] from June 2002 to May 2003 AMSR-E data. The indices are based on mean and standard deviation thresholds applied to 11–19 GHz V polarization TB differences. The snow/ice and RFI flags were transferred to the emissivity database grid by nearest-neighbor resampling. These flagged data locations were not excluded from emissivity retrieval, but the flags are recorded in the emissivity database for use as quality control information when analyzing and interpreting the emissivity data.

[19] To provide sampling throughout the diurnal cycle for analyses of highly penetrating surfaces we used DMSP F13 and F15 SSM/I measurements [*Hollinger et al.*, 1990; *Colton and Poe*, 1999] obtained from the Global Hydrology Resource Center (http://ghrc.msfc.nasa.gov/). The nominal ascending node ECT of the F13 and F15 spacecrafts are 18:33 and 21:05, respectively. SSM/I has V- and H-polarized channels at 19.35, 37, and 85.5 GHz and a V-polarized channel at 22.235 GHz. The nominal EIA is 53.1°. No infrared-derived LST information is available from the DMSP platforms. To support our analyses of SSM/I data, and for comparisons with MODIS LST, we followed *Prigent et al.* [1997] and used the ISCCP DX LST product, which is produced from multiple satellites on a 30 km grid, and is available at 3 h intervals [*Rossow and Schiffer*, 1999; *Rossow and Garder*, 1993a, 1993b].

2.3. Data Processing Flow

[20] Our data processing approach was designed to be flexible with respect to the window of time over which data are processed, with the option of doing a running average of the most recent real-time data to provide dynamic statistics of the local mean and covariance as input to variational algorithms. A correct evaluation of the covariance of surface emissivity estimates is not straightforward because the impact of time variable errors in the input data (infrared surface temperature and atmospheric data) tends to be reduced by averaging while uncertainties due to spatial inhomogeneities and natural variations in emissivity do not. Unless one of these two sources of uncertainties clearly dominates (which is often the case) it is difficult to properly treat their respective contribution in the covariance estimation. When the two contributions are of nearly equal magnitude, one can for instance invoke spectral smoothness constraints (an approach that is particularly effective at 24 GHz) to at least help minimize the impact of atmospheric errors, but a thorough discussion of this aspect is outside of the scope of this paper. The results presented here are monthly mean surface emissivities and total temporal emissivity standard deviations (ESD), recognizing that this metric constitutes an upper bound on the actual level of uncertainty in the emissivity estimate.

[21] With the NPA algorithm, an estimate of T_s for each AMSR-E footprint is produced by averaging the MODIS gridded LST product as weighted by the AMSR-E common spatial response pattern, using a truncated Gaussian function as an approximation. The degree of cloud contamination in the AMSR-E footprint is inferred from the LST quality assessment flags, which avoids the need for processing additional MODIS data sets. In this process, LST data with a claimed uncertainty <3 K are assigned a quality flag of one. Flags for all other data are set to zero. Applying the same spatial averaging process to the quality flags as is used for the LST data results in an estimate of the fraction of clear sky within the AMSR-E footprint, designated here as F_{clear}. A footprint is considered to be "clear" when $F_{clear} \geq 98\%$. The instantaneous emissivities derived through this process are then mapped (together with original AMSR-E brightness temperatures) from swath coordinates to a fixed global sinusoidal grid with 27.8 km spacing (0.25°, for latitude), where each grid point is referenced to the center point of a sinusoidal grid box. In our current implementation, all measurements falling within a 10 km radius of a given grid point are assigned to that grid point. When there is more than one measurement within this radius from a single overpass, the emissivity estimates for a given grid point are averaged and we compute their standard deviation (called local spatial standard deviation: LSSD):

$$LSSD_{\nu,p} = \sqrt{\frac{1}{N}\sum_{i=1}^{N}\left(\varepsilon_{\nu,p} - \bar{\varepsilon}_{\nu,p}\right)^2}, \tag{8}$$

where N corresponds to the number of AMSR-E footprints assigned to the grid point and the overbar refers to the local average. Here we benefit from the high spatial sampling density of AMSR-E products, where N may be as high as 14 at the edge of the scan. This order of processing was selected, rather than mapping TBs to the Earth grid before retrieving $\varepsilon_{\nu,p}$, to minimize retrieval errors associated with inhomogeneities in LST. At high latitudes, sometimes a grid point is sampled on successive orbits on the same day, where the swaths of coverage overlap. In these cases, we retain in our database the data from only the first orbit. Data from ascending and descending (day and night) passes are stored separately.

[22] There are many areas affected by frequent cloudiness and precipitation where the number of clear AMSR-E measurements over the course of one month is insufficient for generating accurate emissivity estimates. One can attempt to populate the frequently cloudy areas by accepting partly cloudy (lower quality) measurements in the process: that is, by progressively relaxing the F_{clear} threshold until the number of available samples is large enough to build a statistically meaningful estimate of the mean emissivity. A quality control (QC) process must be applied to detect and exclude microwave measurements that are highly contaminated by cloud liquid water or precipitation and/or emissivity spectra produced with contaminated LST estimates (erroneously flagged as clear by the MODIS cloud mask). A description of the QC process for NPA retrievals is in section 3. The NPA process builds three temporary gridded data sets with different F_{clear} thresholds: $F_{clear}^{\min}$ = 98%, 50%, and 20%. The local monthly mean emissivity and covariance are derived using the highest $F_{clear}^{\min}$ (from among these choices) for which an adequate sample is obtained, subject to QC on each sample. Day and night data are processed separately. Figure 2 shows the geographical distribution of $F_{clear}^{\min}$ for July 2003. The absence of data in the high latitudes in July is due to the lack of data from the day-night LST algorithm, which relies on diurnal thermal contrast. In these regions, the MODIS

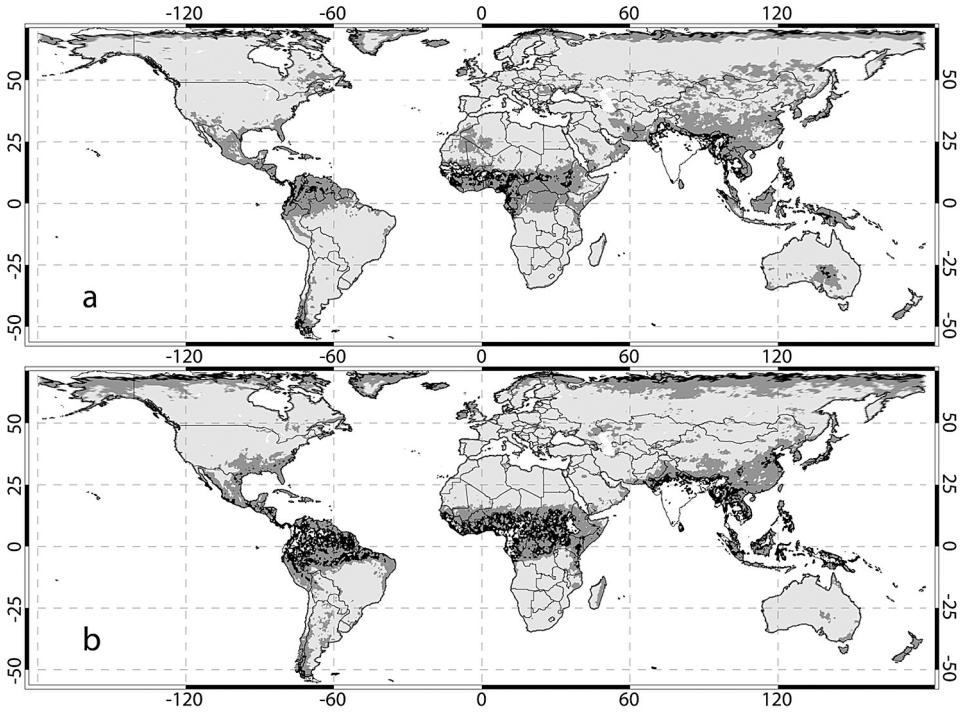

Figure 2. Geographical distribution of grid points where an adequate sample was obtained with $F_{clear}^{\min}$ = 98% (light gray), 50% (dark gray) and 20% (black) for July 2003, and where there was no adequate sample (white), for (a) day and (b) night orbit data.

split window algorithm [*Wan and Dozier*, 1996; *Wan*, 2008] could be used instead. The production of final emissivities over areas affected by persistent cloudiness, such as the equatorial regions, uses an additional step in which we replace cloudy emissivity estimates by estimates from mostly clear areas with compatible surface type. More details about the handling of these areas are given in section 3.4.

[23] Figure 3a shows mean differences between day and night 19V (19 GHz V polarization) emissivity estimates for July 2003, from the NPA process. The large negative differences are attributed to surface penetration effects [*Galantowicz et al.*, 2011], which are quite widespread. With penetration, $T_s > T_e$ at midday, causing (2) to underestimate the emissivity. At night, $T_s < T_e$ and the emissivity is overestimated. Over vegetated areas (Figure 3b) there are no large negative differences. The nonzero (and generally slightly positive) mean day-night differences in vegetated areas may result from cloud contamination or other effects. These effects are treated in the QC process, which was not invoked for producing these maps. One known potential exception is the occurrence of significant positive day-night differences over the U.S. corn belt during the summer months, attributed to frequent nighttime dew deposition on crops. The analysis of this particular case will be the subject of a subsequent paper.

[24] The PTS algorithm is intended for use only over arid and semiarid regions (where microwave penetration is most significant) although we have applied it globally for testing and to tune elements of the approach (and ensure a smooth transition between the NPA and PTS products). For results presented here, the algorithm is applied to solve for a set $\{\varepsilon_V, \varepsilon_H, \alpha\}$ at each frequency to represent day and night for the month. The PTS algorithm requires the use of infrared observations at different times of the day (to characterize the amplitude and phase of the diurnal forcing) and microwave measurements from multiple polar-orbiting satellites. We initially used 3-hourly ISCCP-derived LST, but early comparisons of MODIS and ISCCP products for year 2003 revealed major inconsistencies between the two products (J.-L. Moncet et al., Discrepancies between MODIS and ISCCP land surface temperature products analyzed with microwave measurements, submitted to *Journal of Geophysical Research*, 2010). In particular, it was found that AMSR-E ESD's improve significantly, especially over arid regions, when ISCCP LSTs are replaced with MODIS's in our NPA process. Day-night emissivity differences produced with MODIS LSTs are also more consistent with our knowledge of regional surface characteristics. There is some ongoing parallel effort to determine the causes for the discrepancies between the two LST data sets.

[25] Over densely vegetated areas, cloudiness may be quite frequent and impacts of clouds on radiation at the surface may be such that thermal forcing is not periodic, making it inappropriate to apply the periodic model described by (6). Snow/ice covered surfaces, sparsely vegetated areas affected by intermittent precipitation, or irrigated areas where the state of the surface may be rapidly changing are also problematic for this model. The PTS algorithm has its own QC tests (required for ensuring consistency among multiple satellites and diurnal cycles) and is designed to also make use of the NPA QC flags to isolate time segments where surface emis-

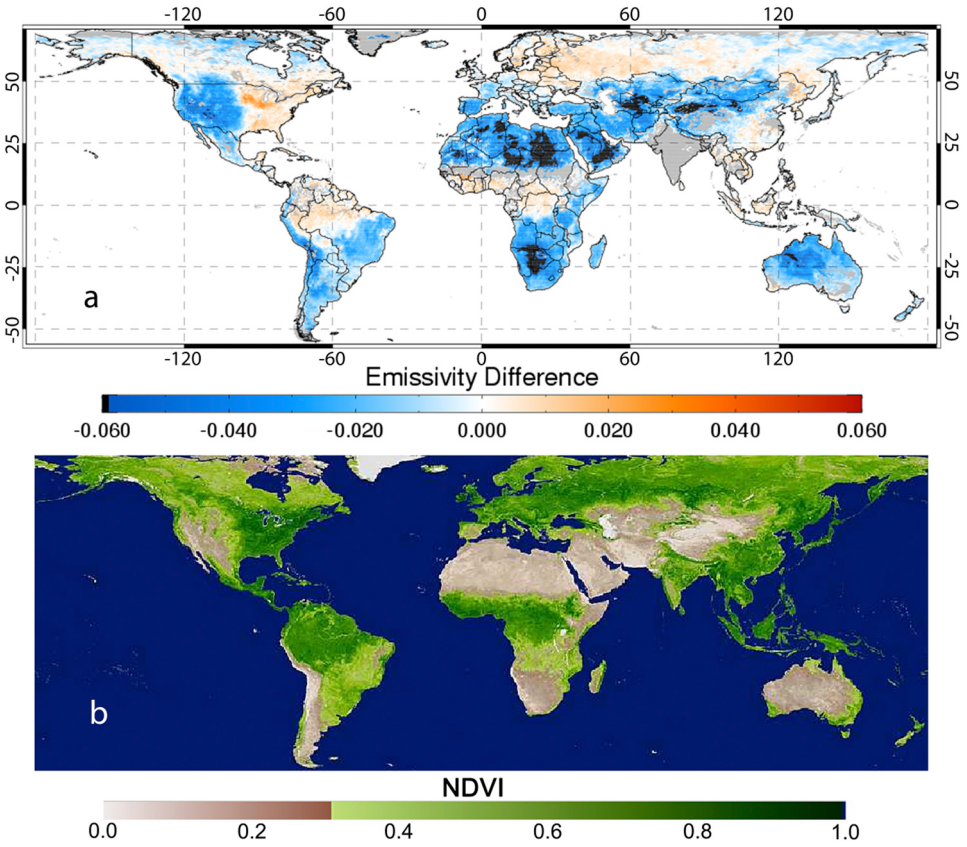

Figure 3. (a) Day-night difference in the July 2003 mean emissivity from the NPA processing for 19V channel and (b) normalized difference vegetation index (NDVI) from MODIS for July 2003 (http://landqa2.nascom.nasa.gov/cgi-bin/browse/browse.cgi [*Roy et al.*, 2002]).

sivity appears stable and to exclude, for example, bad LST estimates. Further analyses of PTS algorithm errors are presented by *Galantowicz et al.* [2011]. Criteria for choosing between the NPA or PTS products at any given grid point are discussed in section 4.

3. Quality Control

[26] Usefulness of emissivity atlases for constraining retrieval of surface temperature and/or atmospheric properties under cloudy conditions is measured in terms of the temporal predictability of surface emissive properties. Observed daily local temporal variability of the retrieved NPA surface emissivities (Figure 4) primarily originates from four sources:

[27] Spatial inhomogeneities: variations in the spatial sampling around a grid point over surfaces containing inhomogeneities on the scale of the AMSR-E footprint introduce day-to-day variations in the spatially averaged emissivities for that grid location. The degree of inhomogeneity is reflected in the LSSD (section 2.3). The spatial inhomogeneities are largest along boundaries of large open water bodies and over snow/ice (Figure 5). Removal of open water contamination from the microwave measurements is left for future enhancement.

[28] RFI: areas of known 11 GHz RFI contamination are currently flagged using a static RFI mask (see section 1). Because areas affected by RFI and the level of contamination in these areas are likely to change with time, work is currently ongoing to derive this mask dynamically from the retrieved NPA emissivities.

[29] Natural (or anthropogenic) variations in the surface properties that are due, for example, to changes in soil moisture or vegetation characteristics.

[30] Errors in the specification of surface temperature and atmospheric terms (mainly cloud liquid water and water vapor) that vary with time.

[31] The QC process described in the rest of this section deals with the last two of these sources. The main objective of the QC process is to remove occasional large errors in the input LST and atmosphere data as well as isolated natural events (such as precipitation) which could have significant impact on the monthly (or other time period) mean and ESD entered in the database. The factors could also induce spurious differences between mean day and night emissivity estimates, which are used as a basis for switching between NPA and PTS algorithms in our merged product (section 4) and are also valuable as diagnostic flags. Isolated natural events are not "bad data," and can be worthy of analysis (such as for building constraints on surface emissivity in precipitating environments), but they are unrepresentative of the more typical state (over time scales of a few weeks) that our emissivity database is intended to provide as background data for retrieval and assimilation (in the form of mean emissivity and ESD). To be consistent, the retrieval/assimilation must include tests for anomalous conditions and

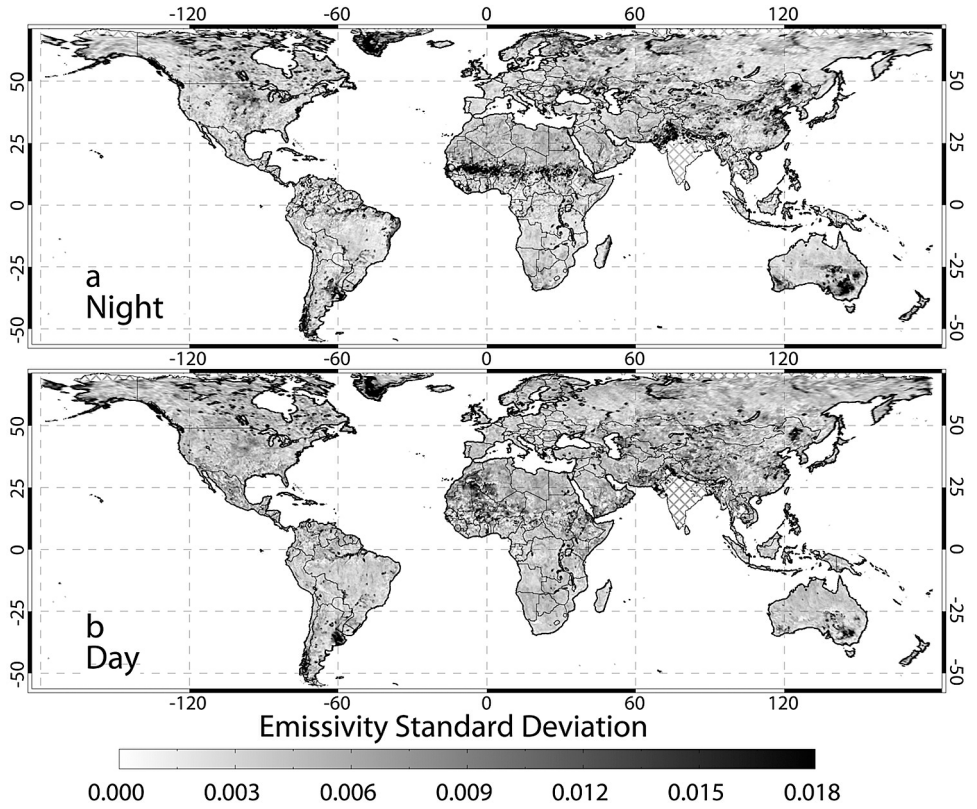

Figure 4. AMSR-E 19V (a) night and (b) day NPA emissivity standard deviation for July 2003, prior to quality control (section 3). Areas with insufficient clear-sky sampling are cross-hatched (e.g., India; Figure 2).

use relaxed background constraints in those circumstances. If we were to retain isolated events in the database along with the typical cases, then the database would not be well tailored to providing background data in either typical or anomalous conditions.

3.1. R11 Filter

[32] The low-frequency channels on AMSR-E are very valuable for monitoring temporal changes in surface properties that affect emissivity. A particularly useful parameter is the 11 GHz polarization ratio,

$$\mathrm{R11} = T^B_{11V}/T^B_{11H}. \tag{9}$$

[33] The 11 GHz channels have little sensitivity to the atmosphere (outside of precipitating clouds) and the ratio is quite insensitive to surface temperature. Our assumption

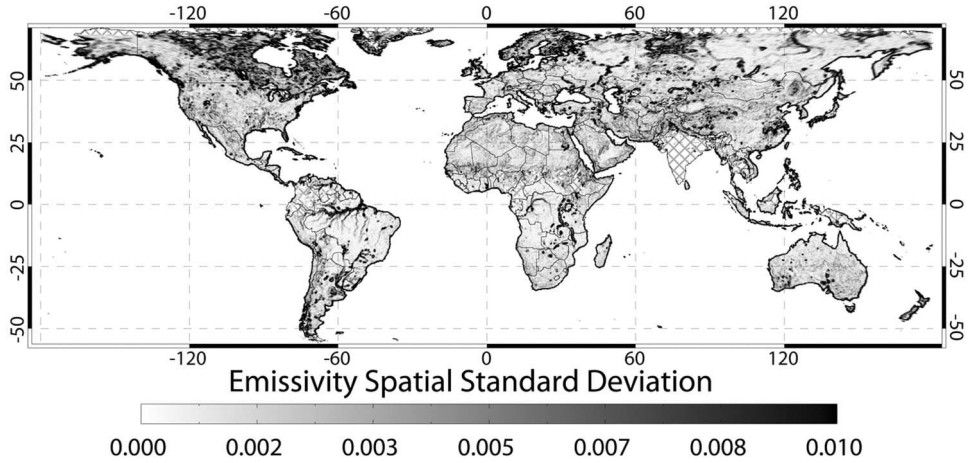

Figure 5. Local spatial standard deviation (LSSD) of 19H emissivity, averaged for July 2003.

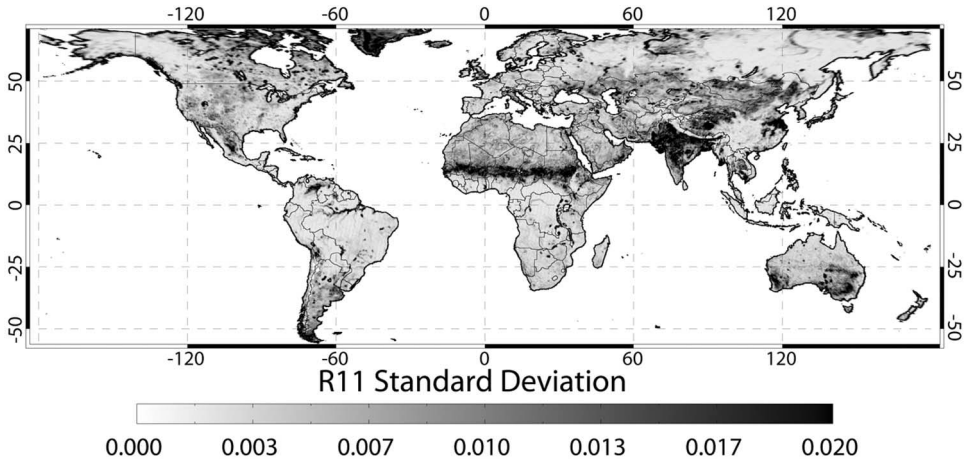

Figure 6. Global map of σ_{R11} for July 2003, night overpass (day map is very similar), including all the available samples, clear and cloudy.

is that analysis of the temporal evolution of R11 would detect most changes in the state of the surface (due to soil moisture, vegetation greening, or harvesting, for example) significantly affecting the surface emissivities at a given location over homogeneous and RFI-free areas. Dew deposition is a phenomenon that potentially affects emissivity and that may not be detectable with R11. This particular phenomenon is being studied separately. Because R11 is insensitive to clouds, it provides continuous monitoring of the surface state (except for days that are unsampled by AMSR-E due to gaps in coverage between swaths from successive orbits, which occurs at low latitudes).

[34] Temporal standard deviations of R11 (σ_{R11}) (Figure 6) tend to be low where the vegetative canopy has high water content and is largely opaque at these frequencies (e.g., forested areas), and in areas where the soil is consistently dry. The regions of highest standard deviation on these scales include sparsely vegetated regions affected by multiple events with precipitation followed by significant drydown (e.g., African Sahel, Southeastern and Southwestern Australia, Northern Argentina, Northeastern China and Northwestern India). These large-scale features are also easily recognizable in maps of ESD (Figure 4), although there are significant differences between the day and night ESD maps (e.g., the Sahel and Australia, where areas of highest ESD occur only at night).

[35] For the current application where the database has monthly statistics, removal of outliers is done by performing an iterated least squares linear fit over all R11 data in the month, governed by a specified threshold of departure of any individual R11 value from the fit line. To provide better time continuity and facilitate the analysis, the algorithm operates on all (clear, partially cloudy, and overcast) AMSR-E measurements. At each iterative step, the most distant outlier from the fit is eliminated, if there are any points beyond the threshold. The threshold to test whether data point $R11_i$ is an outlier is $0.03 \cdot R11_i + \sigma_{sp}(R11_i)$, where $\sigma_{sp}(R11_i)$ is the spatial standard deviation for data point i, similar to the emissivity LSSD (8). The threshold is >0.03 virtually always. The filter is run for day and night data separately and, if the filtered fits are sufficiently similar (as they usually are), the separate fits are replaced by one that operates on day and night data together.

[36] Figure 7 shows maps of 19V ESD before and after R11 filtering in the vicinity of the Intertropical Convergence Zone (ITCZ) in Africa, one of the most challenging regions during the African monsoon. The impact of the filter on the day emissivities (not shown) is small in this particular example. The fact that, prior to filtering, night ESD are often significantly higher than the day ones in this example can be explained by two factors: 1) day conditions following precipitation events are often highly cloudy or overcast and are not included in our emissivity retrieval processing (section 2.3) but night samples during the subsequent dry down correspond to $F_{clear} \geq 20\%$ and are included (Figure 8), and 2) night observations outside of these events are often partly cloudy and retrieved emissivities tend to be more highly cloud contaminated (with cloud detection being less reliable at night). The R11 filter is not designed to deal with cloud contamination effects (unless it occurs concurrently with precipitation events that produce outliers in the R11 time series); nevertheless, the night emissivity standard deviations are much more similar to the day ones after filtering than before filtering (Figure 7). Both day and night ESD remain relatively high in regions where surface characteristics are smoothly but rapidly changing, as well as regions affected by such frequent precipitation that few outliers are detected and excluded.

3.2. Data Error Characteristics

[37] It is apparent from Figure 4 that emissivity variations are small over a large portion of the globe and are commonly very small, even before QC has been applied. When we focus on clear areas with stable surface properties (Figure 9), more than 97% of the points have 19V ESD < 0.01 for both day and night retrievals. For many areas with high F_{clear}, the shape of individual emissivity spectra is remarkably stable over time, with spectrally uniform variations from day to day (Figure 10) indicating that the main cause for emissivity variations is discrepancies between the LST from MODIS and the true $T_{e,\nu}$. Over areas where penetration impact is significant, this uniformity is maintained even as the effec-

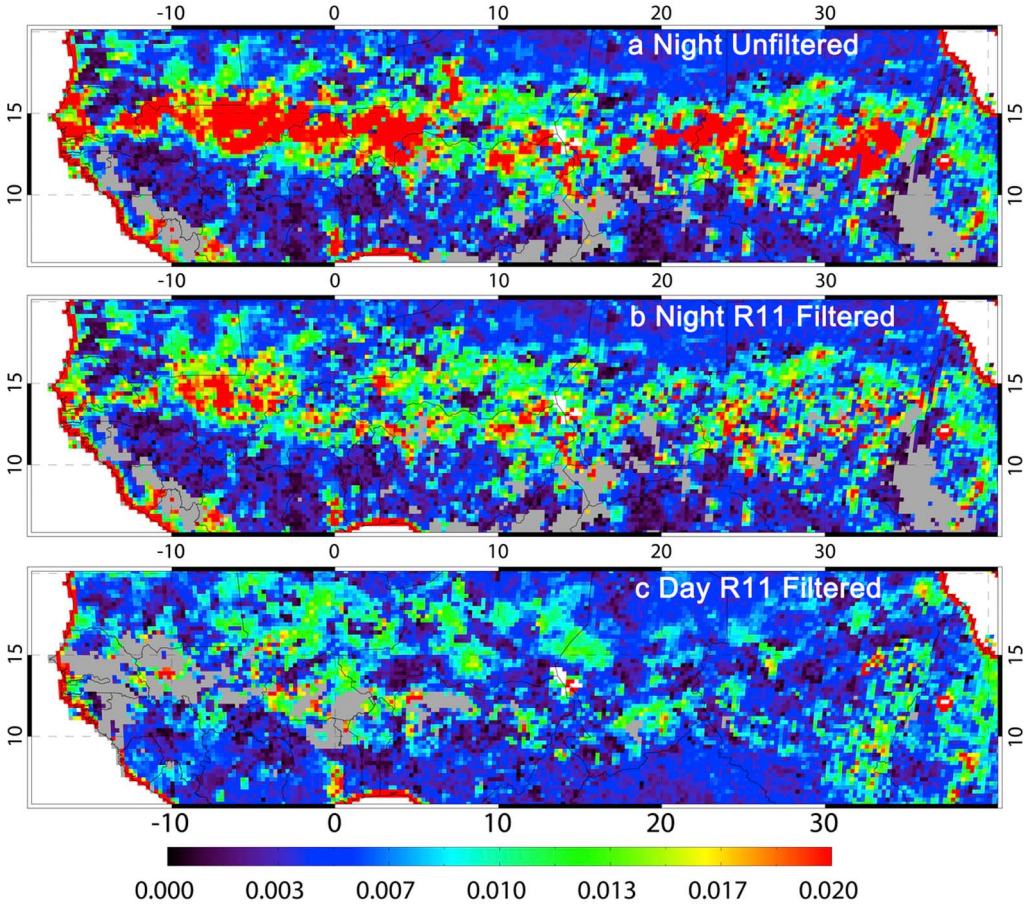

Figure 7. AMSR-E 19V emissivity standard deviation along the ITCZ in Africa in July 2003, for (a) night unfiltered, (b) night R11 filtered, and (c) day R11 filtered emissivities.

tive emissivity (ignoring penetration) changes from day to night at the lower frequencies (Figure 10c). The differences between $T_{e,\nu}$ and T_s (section 2.1) may vary day to day, even in dry areas, when the atmosphere modulates the surface radiative forcing. It is apparent from Figure 9 that the variability introduced by this effect (in combination with other thermal factors) is quite small. The small fluctuations in the retrieved 24 GHz emissivities around a straight line drawn between the 19 and 37 GHz emissivities partly reflect time-varying errors in the NCEP-derived water vapor data. When

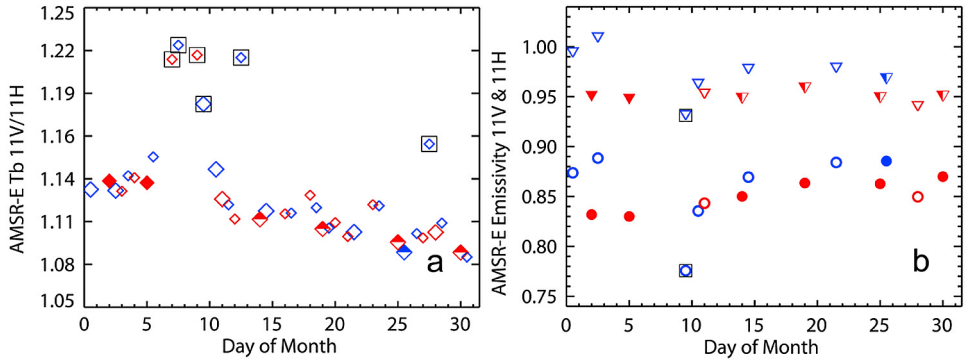

Figure 8. Time series of (a) R11 and (b) retrieved 11 GHz emissivity at polarizations V (triangles) and H (circles) at a grid point at the northern edge of the ITCZ (13.88°N, 12.49°E) from July 2003. Red and blue indicate day and night measurements, respectively. A square indicates outliers according to the automated R11 filter (section 3.1). With R11, F_{clear} is indicated for ≥98% (filled), ≥50% (half filled), ≥20% (empty), and <20% (reduced size and empty). No emissivities are produced for F_{clear} < 20%.

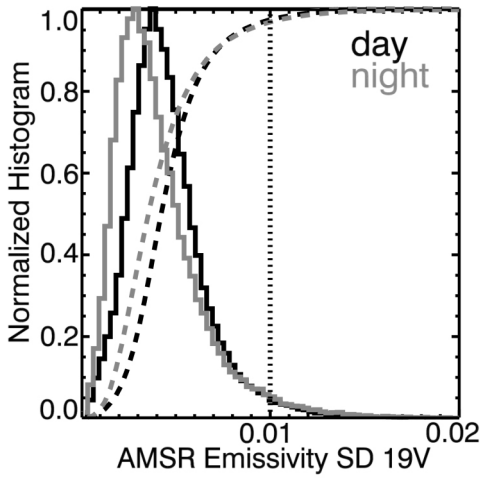

Figure 9. Histograms of 19V ESD for clear areas ($F_{clear} \geq$ 98%) with stable surface properties ($\sigma_{R11} < 0.015$) for July 2003 night and day. The dashed lines are the cumulative frequencies.

applying the emissivity data to atmospheric retrieval, small uncertainties in the 24 GHz emissivity may translate into significant uncertainties in retrieved water vapor amount over highly emissive surfaces. We noted means of correcting the ESD to reduce the contribution of NCEP model errors (section 2.3), but it is always advantageous to seek more reliable sources of atmospheric data. We experimented with replacing the NCEP data with water vapor data produced by the Atmospheric Infrared Sounder (AIRS) on Aqua. We found that the replacement significantly reduces the amplitude of these fluctuations in most cases, but we found instances in which it has the opposite impact. These situations have to be characterized before we are able to deal with them as part of our QC process.

[38] The above results indicate that there are not any large sources of error variation that would have a global effect, and that there is a very high level of temporal consistency between the AMSR-E measurements and the MODIS LST product in clear areas. These results also rule out large instabilities in AMSR-E calibration and geolocation. Problems with control and measurement of the temperature of the AMSR-E warm calibration load have been addressed such that its temperature is believed to be known within 0.5 K, and should introduce <0.002 (rms) uncertainty in the retrieved surface emissivities (F. Wentz, personal communication, 2007). Variations introduced by radiative transfer model errors play a secondary role. Errors due to random instrument noise [*Kawanishi et al.*, 2003] are considered negligible compared to the other sources of errors. Random errors in the MODIS LST product (including errors due to occasional cloud contamination) have their impact significantly reduced by spatially averaging over the AMSR-E footprint (by a factor of ~8 in the clearest footprints).

[39] The main errors occur in partly cloudy areas and result from cloud bias in LST estimate and cloud contamination of infrared measurements as well as liquid water contamination of the microwave measurements. An estimate of T_s derived by averaging the infrared LST data over the clear portion of the microwave sensor footprint may not be representative of the average LST for the entire footprint. These cloud biases vary day to day with cloud cover and cloud optical thickness, and would be larger for lower values of F_{clear}. They would also tend to be larger for drier surfaces, where there is less evaporative conversion of solar heating into latent heat and there is greater response of T_s to the diurnal solar flux. Clouds and aerosols also introduce variations through contamination of the "clear" MODIS LSTs. Under-analysis of cloud cover is expected to occur most frequently at the edges of extensive cloud masses, in the presence of subpixel clouds, with low clouds at night, or with thin cirrus. The most obvious instances of cloud/dust contamination are filtered out in our process (section 2.2) but some contaminated LST data pass through the filters because of the trade-off between removing all possible contaminated LSTs and systematically excluding actual clear regions. More detailed analysis of cloud impacts has revealed the predominance in the daytime data of positive differences in the 19V emissivities between partly cloudy and clear conditions, an indication that LST contamination is the main factor.

[40] Clouds containing significant amounts of liquid water (i.e., >0.02 kg/m^2) and/or large ice crystals may significantly affect the AMSR-E measurements, especially at the higher frequencies [*Gasiewski*, 1993]. In our emissivity retrievals, this effect occurs mainly for measurements at the 50% and 20% thresholds of F_{clear}^{min}, but also where $F_{clear} \geq$ 98%, due to occasional under-analysis of cloud cover. The

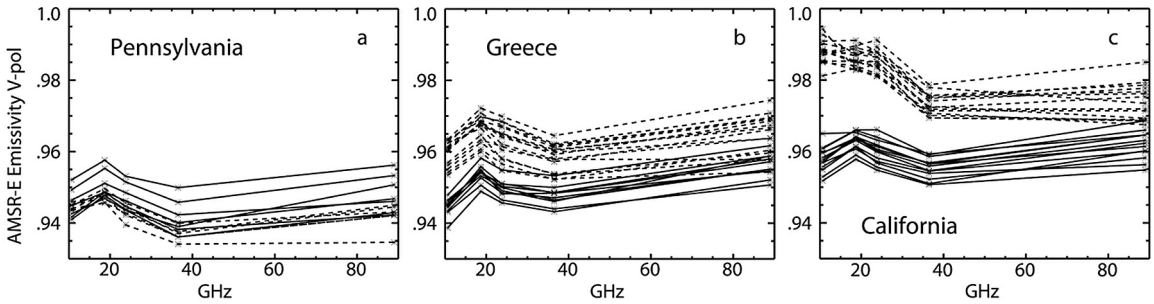

Figure 10. Emissivity spectra (from NPA algorithm) at V-pol for selected grid points. Each line is a daily average, and only spectra with $F_{clear} \geq$ 98% are included. Solid and dashed indicate day and night measurements, respectively.

R11 polarization ratio is essentially insensitive to low to moderate amounts of liquid water over highly emissive surfaces and is, by construction, insensitive to errors in LST.

3.3. Cluster Analysis

[41] We employed a clustering analysis method, which is applied after the R11 filter, with the intention of eliminating emissivity spectra affected by anomalous LST data and occasional (mostly nonprecipitating) cloud-contaminated gridded AMSR-E measurements not removed by the R11 filter. The clustering approach is designed to improve the quality of our emissivity statistics in areas where the probability of clear (or mildly cloud contaminated) measurements is high.

[42] The method operates on the retrieved emissivity spectra, and first operates on the 11V channel to eliminate outliers due to erroneous estimates of LST. The method finds groups where no member is farther than a proximity threshold from its nearest neighbor. The proximity threshold varied with the LSSD. If, for a given threshold $F_{clear}^{\min}$, the number of clusters found is anything other than one or if one cluster is found and the number of members is less than three, then the process incorporates samples up to the next threshold, working in the sequence of $F_{clear}^{\min}$ 98%, 50%, 20%. Once the LST outliers have been excluded, the clustering process is repeated while operating on the spectral offsets of 19V and 37V relative to11V, with the primary effect being elimination of instances of cloud contamination that affect the emissivity spectral slope. Where the full process results in anything other than a single cluster, no monthly emissivity statistics are generated.

[43] In regions of persistent cloudiness, instances where clouds are under-analyzed are not uncommon. It is often better in this case to analyze a larger number of potentially cloud-contaminated samples than few samples wrongly flagged as clear. In the tropics, instances of precipitation or high liquid water/ice contamination are well captured by the clustering scheme but, because truly clear (or mildly cloud contaminated) measurements are scarce, one cannot isolate the least cloud contaminated measurements among the retained samples based on statistics only, and the clustering algorithm is unlikely to produce only one cluster. In such situations, lengthening the averaging time period (wherever emissivities are sufficiently stable) is not expected to improve results, so long as the probability of clear measurements remains roughly unchanged. For this reason we revert to class-based emissivity substitution (section 3.4) in these conditions.

[44] The most ambiguous areas are the regions of transition between desert and densely vegetated areas (e.g., Figure 7), where frequent clouds and emissivity change may coincide. We expect the cluster analysis process to detect no clusters in ambiguous areas, to avoid passing contaminated NPA results, and specifically to avoid producing erroneously negative day-night differences at low frequencies that would trigger inappropriate reliance on the PTS (penetration) algorithm.

3.4. Filling Based on Surface Type Classification

[45] In order to provide emissivity estimates over areas affected by persistent cloudiness, we used emissivity data from grid points that had matching surface types and had more clear measurements. Static surface type data, following the International Geosphere Biosphere Programme (IGBP) classification system, were taken from MODIS products (MOD12Q1, http://www-modis.bu.edu/landcover/userguidelc/lc.html). In the future, the approach may be enhanced by using dynamic data from NDVI composite products (e.g., MOD13Q1) or other sources. Our approach uses R11 data (as described below) to account for the fact that various microwave signatures may occur for a single IGBP surface type and, conversely, various IGBP types have very similar microwave spectra.

[46] The surface type database was regridded to the same locations as the AMSR-E emissivity database, with spatial averaging to obtain the fraction of each grid point for each class (similar to the treatment of the MODIS cloud mask; section 2.3). To develop the correspondence between surface type and AMSR-E emissivities, emissivity monthly mean spectra were stratified by type and by R11 and examined graphically and statistically. We considered the most prevalent two types at each grid point in the stratification. This examination was limited to clear locations ($F_{clear}^{\min} \geq$ 98%) with stable surface conditions ($\sigma_{R11} \leq 0.006$) and latitudes where deciduous trees would be reliably in full leaf (e.g., −25 to 50°N in July and −35 to 25°N in November). Day and night data were handled separately, to allow use of this approach in regions with nonnegligible day-night differences in NPA emissivities.

[47] In the examination of spectra for well-vegetated types, we found no consistent differences in the populations of spectra from different geographical regions, according to broad bands of longitude (e.g., the Americas versus Africa). None of these vegetation classes spanned a large range of latitude. Spectra that were from moderately-heavily vegetated types (primary and secondary class) were generally similar to each other, regardless of the specific type, within each of the lower strata of R11 (R11 < 1.04), but some differences between these types were apparent. The graphical and statistical measures indicated there were four groups according to primary IGBP type: 1) evergreen needleleaf forest, 2) evergreen broadleaf forest + deciduous broadleaf forest, 3) mixed forest, 4) woody savannas + savannas. For some months, evergreen needleleaf forest and mixed forest spectra were very similar to each other, but neither of these were consistently similar to each other through the full year, so they were kept separate. This grouping included only points composed >90% from one or two of these six types. The ranges of R11 were defined so that, within each R11 range for each surface type group, the variation in the monthly average emissivity spectra was comparable or less than the typical day-to-day variability at a single grid point. The selected R11 ranges were 0.99–1.01, 1.01–1.02, 1.02–1.03, and 1.03–1.04, and points with R11 ≥ 1.04 were excluded.

[48] For each of the four groups and ranges of R11, average spectra were computed by pooling all members. Group standard deviations were computed by combining the variation over the month at each site with the variation between sites, while treating all sites as if they had the same number of samples during the month:

$$\sigma_g^2 = \frac{1}{N_g}\sum_{i=1}^{N_g}\sigma_i^2 + \frac{1}{N_g}\sum_{i=1}^{N_g}\overline{\varepsilon}_i^2 - \left(\frac{1}{N_g}\sum_{i=1}^{N_g}\overline{\varepsilon}_i\right)^2, \qquad (10)$$

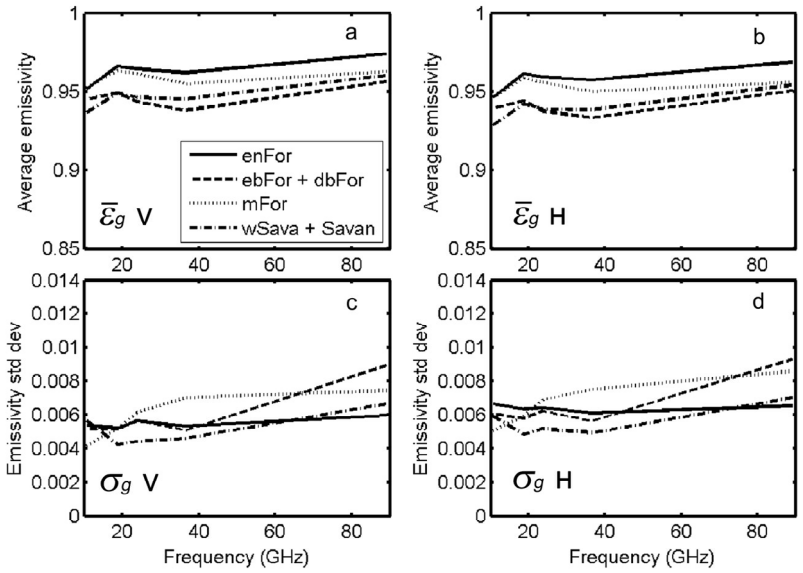

Figure 11. Emissivity statistics by surface type group for day (ascending) overpasses from July 2003 for (a, c) V and (b, d) H polarization, with the group average (Figures 11a and 11b) and standard deviation (Figures 11c and 11d). These data are for the interval $0.99 < R11 < 1.01$. The surface types are discussed in the text.

where $\bar{\varepsilon}_i$ and σ_i are the monthly average and standard deviation at site i, g is the group index, and N_g is the number of sites in a group. An example of the statistics for the range $0.99 < R11 < 1.01$ is in Figure 11, where it is apparent that σ_g is only moderately greater than the typical ESD for individual clear sites (Figure 9). The relatively high values of σ_g at the lowest frequency (11 GHz) for the savanna group are likely due to instances of modest surface penetration. The values of σ_g rise from each range of R11 to the next, where there is more possibility for emissivity to vary as vegetative water decreases and R11 correspondingly increases. For each group and R11 range, the differences between the day and night (not shown) average emissivities were larger than σ_g, even for the forest groups, and the differences increased with range of R11.

[49] The group spectra were inserted in the database at sites that were not clear (no cluster for $F_{clear}^{\min} \geq 98\%$), using the same criteria of type and R11 from which the group statistics were created, for ranges of R11 down to 0.96. An additional criterion was that valid class-based spectra be available for the matching surface type, R11 range, and month. This criterion eliminated a large number of otherwise suitable cases, mostly in spring and fall, when the latitude range being treated was smallest (to ensure exclusion of forests at less than full leaf). This approach was nevertheless able to extend "clear" emissivities considerably beyond what we could obtain without class-based filling (Figure 12). In many of the areas where class-based results were produced, there was little difference between those results and the original, cloudy NPA results (that included spectra with $F_{clear}^{\min} \geq 98\%$) for the monthly average 11V emissivities (not shown), but the 89V emissivities differed substantially (Figure 12d), due to the higher sensitivity to cloud contamination at the higher frequency [*Gasiewski*, 1993]. These changes were often of greater magnitude than the within-group variation (Figures 11c and 11d). Areas where the criteria for producing class-based data were met tended to have high spatial variability in the original products, suggestive of cloud contamination (Figure 12a). In maps of NPA emissivities in which the original, cloudy products were substituted by class-based products wherever they had been produced, the transitions between cloudy (substituted) areas and adjacent clear areas were generally smooth (Figure 12c), which would not occur if the substitutions were highly faulty. In time series of monthly emissivity maps (not shown) there were several instances of spatial and temporal anomalies that were eliminated when this class-based substitution was done (e.g., southern Borneo and New Guinea in Figures 12a and 12c). The most prominent remaining anomalies occurred where class-based products were not available.

4. Merged Products

[50] For a large fraction of the global land grid points, more than one of the algorithm approaches discussed above can produce emissivity products. In addition to the separate databases for the NPA, class-based, and PTS products, a merged product has been generated that represents, on a point-by-point basis, what we consider to be the most reliable estimate of the monthly background emissivities for each AMSR-E channel. The merging process starts with the NPA product as the default. Wherever the criteria for creating class-based emissivities (section 3.4) are met, they override the default. The PTS products are used for all grid points that pass a series of tests for reliability of the PTS retrieval and significance of microwave penetration, considering data sample sizes and measures of the quality of the

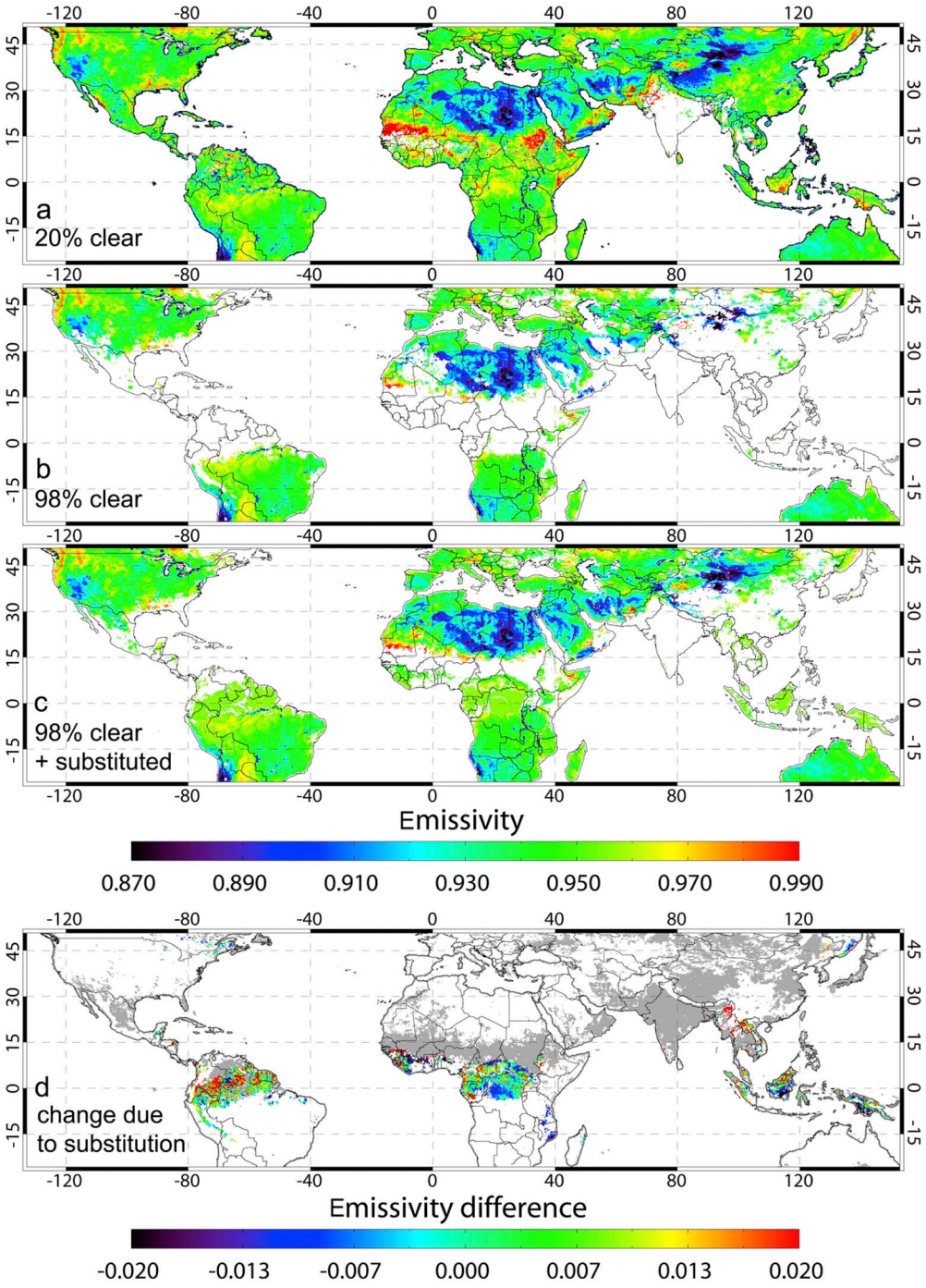

Figure 12. The 89V emissivities from (a) $F_{clear} \geq 20\%$, (b) $F_{clear} \geq 98\%$, (c) combination of $F_{clear} \geq 98\%$ and class-based substitution, and (d) the difference between Figures 12a and 12c. Areas shaded gray in Figure 12d were cloudy ($F_{clear} < 98\%$) but ineligible for substitution due to $\sigma_{R11} > 0.006$.

fit between the data and the penetration model [*Galantowicz et al.*, 2011]. By these criteria, the PTS products are selected for a substantial portion of the global land, responding to arid conditions well beyond deserts. For example, much of Western Europe had significant penetration in August 2003 (Figure 13), during highly anomalous hot and dry conditions [*Bell and Eichler*, 2004].

[51] At grid points where the original NPA or the class-based product is selected, the separate day and night emissivities are averaged to make the merged product. Any systematic differences between day and night emissivities are artifacts of microwave penetration and vertical temperature gradients (section 2.1), and this averaging eliminates the artifacts, subject to the approximation that the penetration-

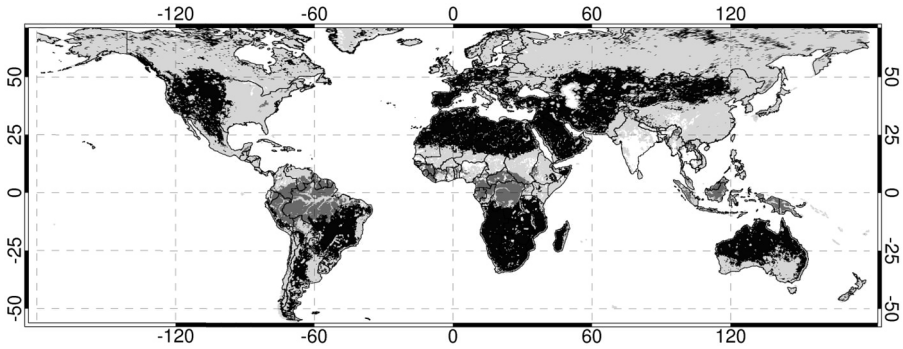

Figure 13. The source of data for the merged product for August 2003 night orbit, based on the selection criteria, for the NPA (light gray), class-based (dark gray) and PTS (black) algorithms, and none (white).

related biases in the day and night emissivities cancel each other. In most locations where the day-night difference is large (and negative), the merger criteria generally result in selection of the PTS product and there is no day-night averaging to be done (according to comparisons of plots such as Figure 3a and Figure 13, when both plots are for the same month).

5. Evaluation and Analysis of Emissivity Products

[52] In section 3 we discussed the consistency between MODIS and AMSR-E measurements over short time scales (less than 1 month). Retrieved instantaneous (NPA) emissivities tend to be very stable over time in some locations and highly variable in other locations. The amount of short-term natural variability varies significantly with season in many locations. According to Figure 14, the percentage of snow-free stable grid points varies from 48% to 73% of the total land surface, depending on the time of the year. The percentage of unstable locations ranges between 10 and 15%. These include coastal areas, agricultural regions and other areas affected by frequent precipitation and rapid changes in vegetation cover. Where the surface is stable per our R11 test, the ESD data provide an upper bound for the magnitude of the time-varying errors entering into our process. The retrieved emissivities may also be affected by biases in the measurements or the ancillary data that vary slowly with time. Since suitable ground truth emissivity data do not exist, we do not have a direct mechanism to assess these biases. Alternative ways to make relevant inferences about these biases are comparison with physical models, assessments of regional interconsistency (e.g., Moncet et al., submitted manuscript, 2010), and analysis of derived data (e.g., surface temperature or atmospheric water vapor retrieved using the emissivities to constrain the surface).

[53] Figure 15 shows maps of the AMSR-E merged product and, for comparison, SSM/I emissivities from a database produced with the heritage nonpenetration method [*Prigent et al.*, 1997]. Focusing on the regions of highest and lowest emissivity for November 2003 south of 42°N (snow-free outside of high elevation regions), many features in the AMSR-E and SSM/I maps are quite similar. Sandy deserts (Arabian, Thar, Karakum and Taklimakan) are easily identifiable in the AMSR-E data by their high emissivity in the 19V channel. The low reflectivity of these bare surfaces may be explained by the fact that they are observed at an angle that is close to the Brewster angle. Vegetation tends to scatter the radiation and therefore lower the emissivity (and polarization difference). In our AMSR-E results, emissivity estimates over the desert areas are produced by the PTS algorithm. The magnitude of the emissivities over the Arabian, Karakum and Taklimakan deserts is similar in the two data sets for November (while the Thar Desert over the Indian subcontinent is not as distinct in the SSM/I data set). Regions with the lowest emissivities in the two data sets also agree well, generally corresponding to regions where water is abundant (Bangladesh, Yangtze and Indus River valleys, and vicinity of major rivers and lakes) but also snow covered or permafrost areas of Tibet.

[54] The data sets differ significantly over most arid regions for June, where the SSM/I database has much lower emissivities. Emissivities over sandy deserts in this SSM/I

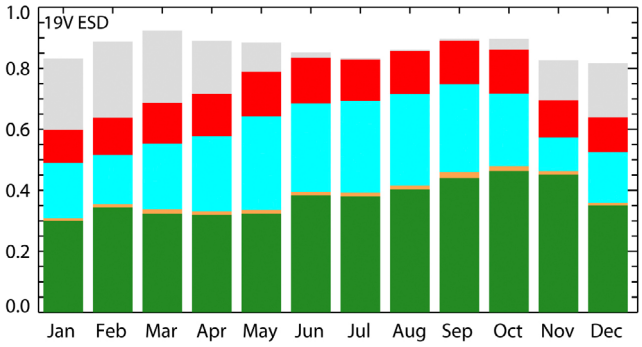

Figure 14. Fraction of grid points in final database, for all the months of 2003, with conditions specified by color. Green: $\sigma_{R11} < 0.015$, ESD < 0.01, NPA; orange: $\sigma_{R11} < 0.015$, ESD ≥ 0.01, NPA; cyan: PTS; red: $\sigma_{R11} > 0.015$; gray: snow. Points not shown in color correspond to polar regions for which no LST estimates from the MODIS day-night algorithm are available (coverage in these regions is minimum in the winter and summer seasons) and points for which no NPA emissivity could be produced. Total 199,525 land grid points.

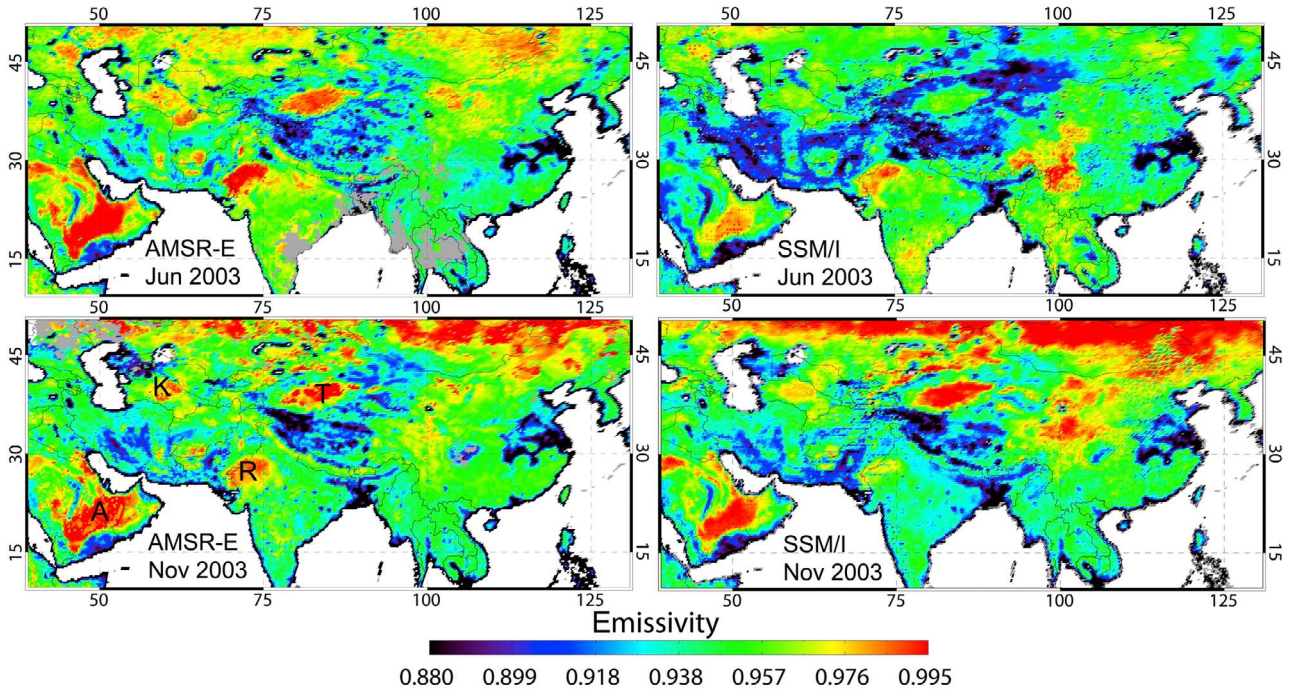

Figure 15. Maps of monthly AMSR-E and SSM/I 19V emissivity over Asia for June and November 2003, as labeled. Deserts discussed in the text are marked A, Arabian; R, Thar; K, Karakum, and T, Taklimakan in Figure 15 (bottom left).

database drop locally below ~0.97 in June (with exception of the Thar desert, which is more distinct in June than November). In addition, very extensive areas over South Central Asia (Iraq, Iran, Afghanistan) and Western China have emissivities approaching 0.90, whereas good agreement between the two databases is maintained over highly vegetated surfaces of, for example, Eastern China, Southeast Asia, and the Indian Peninsula at the beginning and after the wet monsoon. The patch of high emissivity in the SSM/I June map over Southern China (north of the Burmese border) is not clearly associated with any geographic feature and may be an artifact of data errors. By comparison, the emissivities in the AMSR-E maps remain steadier over the arid regions over the course of the year, which is consistent with a lack of seasonal vegetation growth cycle (confirmed by inspection of AMSR-E R11 time series). The large month-to-month differences in these SSM/I data are probably artificial and may result from seasonal/regional biases in the ISCCP LST product (Moncet et al., submitted manuscript, 2010) used to generate these emissivities and thermal gradient contamination of the estimated SSM/I emissivities (produced with a nonpenetration algorithm) over the more highly penetrating surfaces. In our AMSR-E results, the impact of surface penetration, which is most significant around the time of the Aqua satellite overpass, are minimized by detecting regions of high penetration and relying on the PTS algorithm in those regions. The lack of a pronounced seasonal variability over arid and semiarid surfaces in the AMSR-E maps is an indication of the skill of the PTS algorithm for separating thermal effects from surface emission properties.

[55] Detailed inspection of our retrieved AMSR-E emissivities has revealed the presence of systematic anomalies that may be related to instrument calibration errors. Figure 16 shows samples of retrieved AMSR-E emissivities over tropical forest. The emissivities of forest canopies are expected to vary smoothly with frequency in the 11–37 GHz range [*Brown and Ruf* 2005, *Isaacs et al.*, 1989], but the 19 GHz emissivity is high relative to alignment of the 11, 24 and 37 GHz emissivities. In addition, the average differences

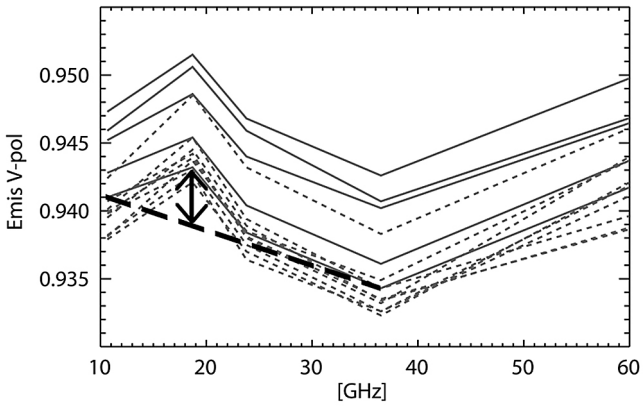

Figure 16. Typical tropical forest emissivity spectra retrieved from AMSR-E in the daytime (solid) and nighttime (dashed). The thick dashed line shows the degree of alignment of the 11, 24, and 37 GHz V emissivities.

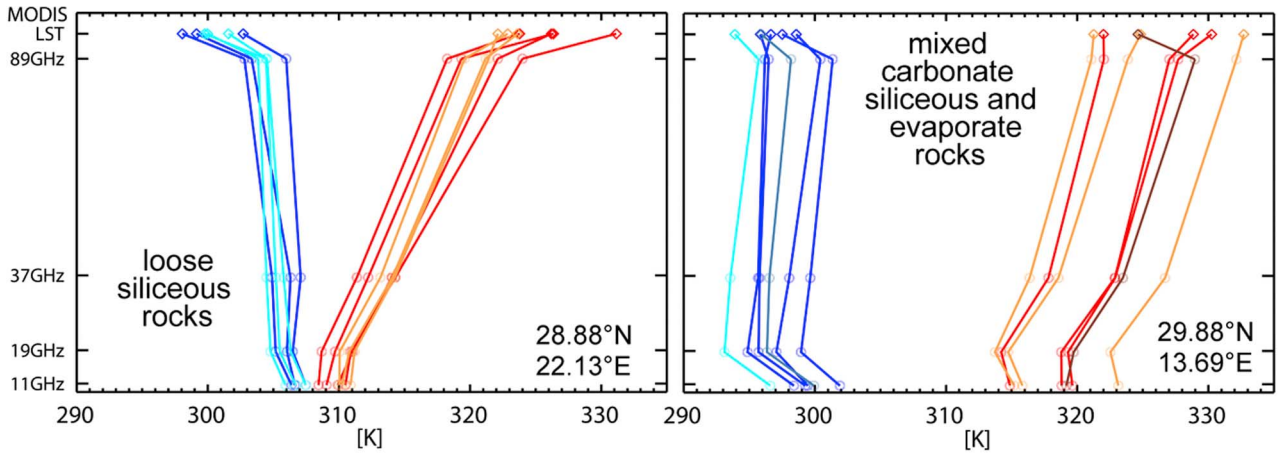

Figure 17. Examples of emission temperature profiles (night in blue and day in red) retrieved for two locations in Libya for July 2003. MODIS skin temperature measurements are indicated by the diamonds. F_{clear} is indicated for ≥98% (red and blue), ≥50% (orange and cyan), and ≥20% (brown).

between 89V and 37V emissivities (not shown) are higher for AMSR-E than SSM/I, indicating a potential high bias at 89 GHz for AMSR-E. *Meissner and Wentz* [2010] recently compared AMSR-E and Windsat measurements over the Amazon and African forests and found that the two sets of measurements agreed very closely at 6, 11, 24, and 37 GHz, but the 19 GHz AMSR-E TBs were 2–2.5 K warmer than the corresponding Windsat measurements, which is consistent with the 19 GHz emissivity anomaly in Figure 16.

[56] In sections 2 and 3, we have discussed the effect of subsurface penetration over arid areas. To our knowledge, this effect has not been taken into account in the previous development of microwave surface temperature algorithms and its impact on surface temperature estimates would have to be quantified. Subsurface penetration may also have implications on the way surface parameters are treated in variational retrieval/assimilation. Figure 17 shows examples of retrieved emission temperature profiles in Libya during July 2003. These profiles were obtained by fixing the surface emissivity spectrum to the monthly values estimated using our PTS algorithm and adjusting $T_{e,\nu}$ to fit the atmosphere-corrected daily AMSR-E observations. This approach is justified based on the fact that R11 does not vary significantly across the month at these locations. The surface at the first location is composed of sand. The subsurface penetration is fairly large over this area leading to positive temperature differences of 10–12 K between the 89 GHz and the more deeply penetrating 19 GHz measurements during the day. MODIS skin temperatures are also significantly higher than the 89 GHz temperatures, suggesting that the 89 GHz penetration is significant over sand. The measurements are very regular from day to day. As expected, the emission temperature contrast between 89 GHz and 19 GHz is generally negative and somewhat smaller in magnitude at night. The temperatures at the second site, which is composed of mixed rocks, have weaker vertical gradients and, in particular, the day contrast between 89 GHz emission temperatures and MODIS skin temperatures tend to be much smaller than over the first site. Day-to-day surface temperature variations as well as diurnal cycle amplitude are also larger at the lower frequencies for the second site than the first. These differences in the retrieved subsurface emission temperatures at the two sites are consistent with lower microwave penetration over rocks than over sand [e.g., *Galantowicz et al.*, 2011].

[57] Maps of monthly mean 89–19 GHz emission temperature differences (Figure 18) show that the magnitude of these temperature differences correlate well with the surface lithology despite heterogeneous weather forcing and clear-sky sampling across the region, which are effectively filtered out in PTS algorithm emissivities (e.g., Figure 18b). In particular, the lowest 89–19 GHz nighttime temperature gradients (i.e., the most strongly negative) clearly coincide with sandy deserts and regions where siliceous rocks dominate (easily identified in the infrared by their low 8.55 μm emissivity, Figure 18c), providing some degree of confidence in the results produced by our PTS algorithm. We would expect the gradients to be near zero in the areas without significant microwave penetration, and we suspect that the significantly positive computed 89–19 GHz temperature differences at night in these areas, including the Northwestern Libya site (Figure 17, right), are nonphysical and may be an artifact of overall positive biases linked to the potential AMSR-E calibration problems described above.

[58] The magnitude of the temperature gradients shown here is such that the use of a single temperature to represent microwave emission at all frequencies is not valid over deserts at least for sensors on a midday orbit. Although emissivity is usually adjusted to partially compensate for the lack of explicit treatment of the spectral dependence of emission temperature, the retrieval problem should be better constrained by using the available a priori knowledge supplied by the PTS emissivities and letting the soil temperature profile be adjusted at least in homogeneous, time-stable regions. This soil temperature profile approach would be particularly beneficial under cloudy conditions, when consid-

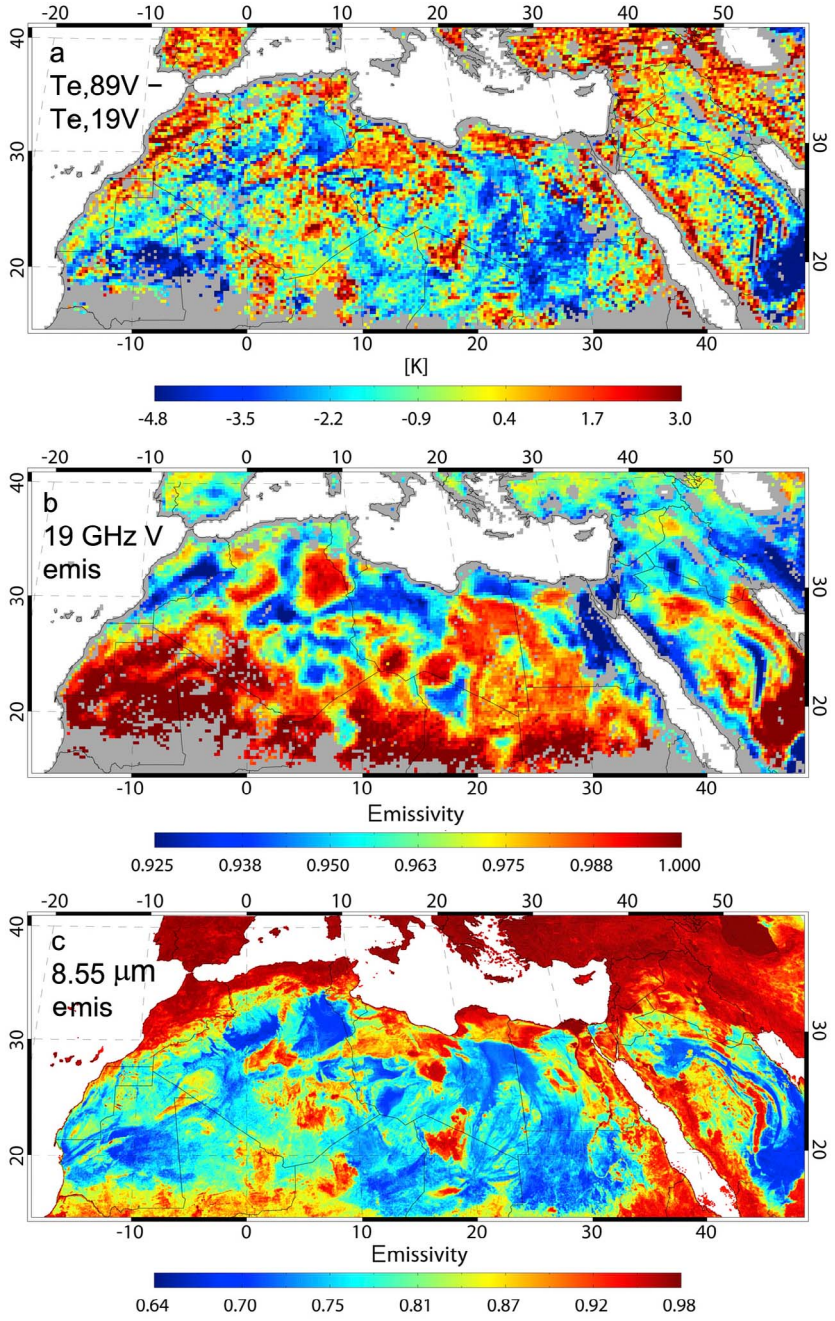

Figure 18. For July 2003: (a) month-average nighttime effective emitting temperature ($T_{e,\nu}$) differences between 89 GHz and 19 GHz in V polarization from the PTS algorithm, (b) 19 GHz V polarization emissivity from the PTS algorithm, and (c) MODIS 8.55 μm emissivity.

ering the large impact clouds can have on the soil thermal structure.

6. Conclusion

[59] The new microwave land surface emissivity database described in this paper is of advanced quality, with respect to minimization of error sources and filtering to eliminate unrepresentative samples. The primary data source was Aqua AMSR-E radiometric measurements, but the database is intended to be used in the future to provide surface emissivity constraints in retrieval or assimilation applications with any conical scanners at frequencies close to the AMSR-E frequencies and V and H polarizations. In this case, some correction is needed to deal with slight differences in viewing angle, and the potential biases related to instrument calibration highlighted in this paper would need to be corrected. An essential factor in the database quality is the availability and use of well-collocated, radiometrically consistent clear-sky MODIS LST as ancillary data for the emissivity retrieval.

Good temporal and spatial collocation is critical for midday measurements (Aqua ascending orbit), when surface temperatures are rapidly changing and where spatial heterogeneities are high. The collocation is also critical for getting timely cloud cover estimates used for quality control of the LST data and the AMSR-E measurements. The fact that temporal standard deviation of the departure of our clear-sky surface emissivity estimates from their monthly means is less than 0.005 over 80% of vegetated surfaces is an indication of the high degree of coherence between MODIS derived LSTs and the microwave measurements on the AMSR-E spatial scales. An additional important factor was the use of the 11 GHz brightness temperature polarization ratio to monitor natural surface changes, including abrupt changes associated with rain events, and to separate these changes from temporally variable errors. Over predominantly clear regions with stable surface properties, the precision of analysis is such that 99% of the grid points have 19V emissivity temporal standard deviations (evaluated over monthly periods) <0.01 (Figure 9), compared to 60% for SSM/I processed with ISCCP LST [*Prigent et al.*, 2006]. A detailed analysis of LST source differences and their impacts on emissivity retrieval is presented by Moncet et al. (submitted manuscript, 2010). This particular analysis illustrates an unintended application of our methodology, namely assessment of the quality of independent sources of surface temperature or atmospheric data by analysis of temporal variability of retrieved NPA land surface emissivities over stable surfaces as well as interregional consistency of mean emissivities between regions with the same surface type. The same method is being applied to compare AIRS and NCEP atmospheric products and could be extended to help with microwave sensor intercalibration.

[60] Comparisons of day and night retrieved emissivities suggest that microwave penetration through subsurface layers is a more widespread and substantial factor in interpretation of passive microwave measurements than had been previously established. The timing of the Aqua orbit, in distinction from the heritage sensors, made this finding possible by roughly coinciding with the diurnal maximum of vertical temperature gradients that correspond with the radiometric signatures of the penetration. In a separate paper [*Galantowicz et al.*, 2011], we present strong evidence that penetration is responsible for the day-night differences in apparent emissivities presented here. We extended a thermal model time series fitting approach, originally developed by *Prigent et al.* [1999], to provide emissivity estimates for highly penetrating surfaces that account for the penetration phenomenon, while producing metrics of the microwave effective emission depths as a by-product.

[61] The primary intended purpose of the database is to provide location and time-specific background constraints for variational analysis and assimilation of LST, water vapor, and cloud liquid water in cloudy areas. Minimizing the uncertainty of emissivities is essential to the skill with which these variables can be analyzed. The database is also intended as a dynamic indicator of land surface properties relevant to climate change monitoring. With the current monthly average database, dynamics can be monitored only on seasonal and longer time scales, but we are exploring revised processing methods that allow dynamics on shorter time scales to be analyzed, including transient conditions. In database development, we put a very high priority on quality control, because the value of the database is highly dependent on the precision and reliability of its products. The quality control measures extended from selecting and screening the input data, through the emissivity retrieval algorithm, and to the development of quality flags. The advances collectively constitute a substantial step forward in global monitoring of microwave land surface emissivities from space and the potential for use of satellite derived products in satellite data analysis and assimilation over land.

[62] In limited tests with version 5 of the MODIS LST product, which incorporates version 5 of the MODIS cloud mask, we found no significant, consistent evidence of improvement in the emissivity retrievals. In future work, we hope to be able to improve the quality of the ancillary water vapor estimates by using satellite products from MODIS or AIRS as a replacement for the NCEP/GDAS analysis products as well as the coverage by refining our time segmentation strategy. Recalibration of the AMSR-E instrument is also ongoing (F. Wentz, personal communication, 2010). We are also planning to continue tracking anomalies related to short and long-term stability of surface emissivity estimates, emissivity outliers or day-night or regional biases. For instance, one recent study provides evidence that positive day-night emissivity difference in the Midwest during summer month is related to frequent dew deposition.

[63] **Acknowledgments.** This paper is based upon work supported by the National Aeronautics and Space Administration under contract NNH04CC43C issued through the Science Mission Directorate. We thank Z. Wan of the University of California at Santa Barbara for providing information about MODIS LST data, and for providing software for cloud filtering. Yuguang He performed software development in support of this work.

References

Ackerman, S. A., K. I. Strabala, W. P. Menzel, R. A. Frey, C. C. Moeller, and L. E. Gumley (1998), Discriminating clear sky from clouds with MODIS, *J. Geophys. Res.*, *103*, 32,141–32,157, doi:10.1029/1998JD200032.

Ackerman, S., K. Strabala, P. Menzel, R. Frey, C. Moeller, L. Gumley, B. Baum, S. W. Seemann, and H. Zhang (2006), Discriminating clear-sky from cloud with MODIS: Algorithm theoretical basis document (MOD35), version 5.0, NASA Goddard Space Flight Cent., Greenbelt, Md. [Available at http://modis.gsfc.nasa.gov/data/atbd/atbd_mod06.pdf]

Ashcroft, P. D., and F. J. Wentz (2000) AMSR level 2A Algorithm, *Rep. 121599B-1*, *Remote Sens. Syst.*, 29 pp., Santa Rosa, Calif. [Available at http://eospso.gsfc.nasa.gov/_homepage/for_scientists/atbd/docs/AMSR/atbd-amsr-level2A.pdf.]

Ashcroft, P., and F. Wentz (2003), AMSR-E/Aqua L2A global swath spatially resampled brightness temperatures (Tb) V002, January to December 2003, http://nsidc.org/data/docs/daac/ae_l2a_tbs.gd.html, Natl. Snow and Ice Data Cent., Boulder, Colo. [Updated daily.]

Bell, G., and T. Eichler (2004), Europe: Summer heat wave, in *State of the Climate in 2003*, edited by D. H. Levinson and A. M. Waple, *Bull. Am. Meteorol. Soc.*, 85, S46–S48.

Brown, S. T., and C. S. Ruf (2005), Determination of an Amazon hot reference target for the on-orbit calibration of microwave radiometers, *J. Atmos. Oceanic Technol.*, *22*, 1340–1352, doi:10.1175/JTECH1769.1.

Colton, M. C., and G. A. Poe (1999), Intersensor calibration of DMSP SSM/I's: F-8 to F-14, 1987–1997, *IEEE Trans. Geosci. Remote Sens.*, *37*, 418–439, doi:10.1109/36.739079.

Galantowicz, J. F., J.-L. Moncet, P. Liang, A. E. Lipton, G. Uymin, C. Prigent, and C. Grassotti (2011), Subsurface emission effects in AMSR-E measurements: Implications for land surface microwave emissivity retrieval, *J. Geophys. Res.*, doi:10.1029/2010JD015431, in press.

Gasiewski, A. J. (1993), Microwave radiative transfer in hydrometors, in *Atmospheric Remote Sensing by Microwave Radiometry*, edited by M. A. Janssen, pp. 91–144, John Wiley, New York.

Hollinger, J. P., J. L. Peirce, and G. A. Poe (1990), SSM/I instrument evaluation, *IEEE Trans. Geosci. Remote Sens.*, *28*, 781–790, doi:10.1109/36.58964.

Isaacs, R. G., Y.-Q. Jin, R. D. Worsham, G. Deblonde, and V. J. Falcone Jr. (1989), The RADTRAN microwave surface emission models, *IEEE Trans. Geosci. Remote Sens.*, *27*, 433–440, doi:10.1109/36.29563.

Kalnay, E., M. Kanamitsu, and W. E. Baker (1990), Global numerical weather prediction at the National Meteorological Center, *Bull. Am. Meteorol. Soc.*, *71*, 1410–1428, doi:10.1175/1520-0477(1990)071<1410:GNWPAT>2.0.CO;2.

Kanamitsu, M. (1989), Description of the NMC global data assimilation and forecast system, *Weather Forecast.*, *4*, 335–342, doi:10.1175/1520-0434(1989)004<0335:DOTNGD>2.0.CO;2.

Karbou, F., and C. Prigent (2005), Calculation of microwave land surface emissivity from satellite observations: Validity of the specular approximation over snow-free surfaces?, *IEEE Geosci. Remote Sens. Lett.*, *2*, 311–314, doi:10.1109/LGRS.2005.847932.

Kawanishi, T., T. Sezai, Y. Ito, K. Imaoka, T. Takeshima, Y. Ishido, A. Shibata, M. Miura, H. Inahata, and R. W. Spencer (2003), The Advanced Microwave Scanning Radiometer for the Earth Observing System (AMSR-E), NASDA's contribution to the EOS for global energy and water cycle studies, *IEEE Trans. Geosci. Remote Sens.*, *41*, 184–194, doi:10.1109/TGRS.2002.808331.

Kelly, R. E. J., A. T. C. Chang, and J. L. Foster (2004), AMSR-E/Aqua daily L3 global snow water equivalent EASE-Grids V001, June 2002 to present, http://nsidc.org/data/amsre/data_versions/version1.html, Natl. Snow and Ice Data Cent., Boulder, Colo. [Updated daily.]

Liebe, H. J., P. W. Rosenkranz, and G. A. Hufford (1992), Atmospheric 60-GHz oxygen spectrum: New laboratory measurements and line parameters, *J. Quant. Spectrosc. Radiat. Transfer*, *48*, 629–643, doi:10.1016/0022-4073(92)90127-P.

Meissner, T., and F. J. Wentz (2010), Intercalibration of AMSR-E and Windsat brightness temperature measurements over land scenes, paper presented at 11th Specialist Meeting on Microwave Radiometry and Remote Sensing of the Environment, Inst. of Electr. and Electron. Eng., Washington, D. C.

Njoku, E. G., P. Ashcroft, T. K. Chan, and L. Li (2005), Global survey and statistics of radio-frequency interference in AMSR-E land observations, *IEEE Trans. Geosci. Remote Sens.*, *43*, 938–947, doi:10.1109/TGRS.2004.837507.

Payne, V. H., J. S. Delamere, K. E. Cady-Pereira, R. R. Gamache, J.-L. Moncet, E. J. Mlawer, and S. A. Clough (2008), Air-broadened half-widths of the 22- and 183-GHz water-vapor lines, *IEEE Trans. Geosci. Remote Sens.*, *46*, 3601–3617, doi:10.1109/TGRS.2008.2002435.

Prigent, C., W. B. Rossow, and E. Matthews (1997), Microwave land surface emissivities estimated from SSM/I observations, *J. Geophys. Res.*, *102*, 21,867–21,890, doi:10.1029/97JD01360.

Prigent, C., W. B. Rossow, E. Matthews, and B. Marticorena (1999), Microwave radiometer signatures of different surface types in deserts, *J. Geophys. Res.*, *104*(D10), 12,147–12,158, doi:10.1029/1999JD900153.

Prigent, C., F. Aires, and W. B. Rossow (2006), Land surface microwave emissivities over the globe for a decade, *Bull. Am. Meteorol. Soc.*, *87*, 1573–1584, doi:10.1175/BAMS-87-11-1573.

Rosenkranz, P. W. (1998), Water vapor microwave continuum absorption: A comparison of measurements and models, *Radio Sci.*, *33*, 919–928, doi:10.1029/98RS01182.

Rossow, W. B., and L. C. Garder (1993a), Cloud detection using satellite measurements of infrared and visible radiances for ISCCP, *J. Clim.*, *6*, 2341–2369, doi:10.1175/1520-0442(1993)006<2341:CDUSMO>2.0.CO;2.

Rossow, W. B., and L. C. Garder (1993b), Validation of ISCCP cloud detections, *J. Clim.*, *6*, 2370–2393, doi:10.1175/1520-0442(1993)006<2370:VOICD>2.0.CO;2.

Rossow, W. B., and R. A. Schiffer (1999), Advances in understanding clouds from ISCCP, *Bull. Am. Meteorol. Soc.*, *80*, 2261–2287, doi:10.1175/1520-0477(1999)080<2261:AIUCFI>2.0.CO;2.

Roy, D. P., J. S. Borak, S. Devadiga, R. E. Wolfe, M. Zheng, and J. Descloitres (2002), The MODIS land product quality assessment approach, *Remote Sens. Environ.*, *83*, 62–76, doi:10.1016/S0034-4257(02)00087-1.

Smith, C., F. Wentz, and T. Meissner (2001), Algorithm Theoretical Basis Document (ATBD) for the Conical-Scanning Microwave Imager/Sounder (CMIS) Environmental Data Records (EDRs) Volume 14: Ocean EDR Algorithm Suite, *RSS Tech. Rep. 011001*, Boeing Satell. Syst., El Segundo, Calif. [Available at http://www.aer.com/news-events/resource-library/algorithm-theoretical-basis-document-conically-scanning-microwave-image.]

Wan, Z. (1999), MODIS land-surface temperature algorithm theoretical basis document, version 3.3, NASA Goddard Space Flight Cent., Greenbelt, Md. [Available at http://modis.gsfc.nasa.gov/data/atbd/atbd_mod11.pdf.]

Wan, Z. (2008), New refinements and validation of the MODIS land-surface temperature/emissivity products, *Remote Sens. Environ.*, *112*, 59–74, doi:10.1016/j.rse.2006.06.026.

Wan, Z., and J. Dozier (1996), A generalized split-window algorithm for retrieving land-surface temperature from space, *IEEE Trans. Geosci. Remote Sens.*, *34*, 892–905, doi:10.1109/36.508406.

J. F. Galantowicz, P. Liang, A. E. Lipton, J.-L. Moncet, and G. Uymin, Atmospheric and Environmental Research, Inc., 131 Hartwell Ave., Lexington, MA 02421-3126, USA. (jmoncet@aer.com)

C. Grassotti, I.M. Systems Group, Inc., Center for Satellite Applications and Research, NESDIS, NOAA, Rm. 810, 5200 Auth Rd., Camp Springs, MD 20746, USA.

C. Prigent, Laboratoire d'Etudes du Rayonnement et de la Matière en Astrophysique, CNRS, Observatoire de Paris, 61, avenue de l'Observatoire, F-75014 Paris, France.